



UPPSALA
UNIVERSITET

*Digital Comprehensive Summaries of Uppsala Dissertations
from the Faculty of Science and Technology 1609*

Cutting Edge Titanium-based CVD Hard Coatings

LINUS VON FIEANDT



ACTA
UNIVERSITATIS
UPSALIENSIS
UPPSALA
2018

ISSN 1651-6214
ISBN 978-91-513-0184-6
urn:nbn:se:uu:diva-335907

Dissertation presented at Uppsala University to be publicly examined in Polhemssalen, Ångströmlaboratoriet, Lägerhyddsvägen 1, Uppsala, Friday, 2 February 2018 at 09:15 for the degree of Doctor of Philosophy. The examination will be conducted in English. Faculty examiner: Dr. Henrik Pedersen (Linköping University).

Abstract

von Fieandt, L. 2018. Cutting Edge Titanium-based CVD Hard Coatings. *Digital Comprehensive Summaries of Uppsala Dissertations from the Faculty of Science and Technology* 1609. 77 pp. Uppsala: Acta Universitatis Upsaliensis. ISBN 978-91-513-0184-6.

Modern tools for metal cutting applications, such as turning or milling, are typically improved with a thin protective coating. Despite being only a few microns thick, the coating can increase the lifetime of the tool by more than 100 times compared to an uncoated tool. Two different types of techniques are normally used to deposit the coatings, i.e. chemical vapor deposition (CVD) or physical vapor deposition (PVD). A CVD coated tool often includes several different layers. TiN-Ti(C,N)-Al₂O₃-TiN is a common combination. The research in this thesis has focused on deposition, characterization, and optimization of TiN and Ti(C,N) layers. CVD has been used to deposit all coatings studied in this thesis. They were characterized with a variety of techniques such as: X-ray diffraction, electron microscopy and X-ray photoelectron spectroscopy.

TiN was deposited on three different substrates, Co, Fe and Ni. It was found that the TiN coating was strongly affected by the substrate. TiN deposited on Fe substrates resulted in a porous interface caused by substrate etching by the reaction gas mixture. CVD of TiN on Ni substrates resulted in an unwanted intermetallic phase (Ni₃Ti) in addition to TiN. Etching or corrosion of the Fe substrates could be reduced by lowering the deposition temperature. In addition, the formation of (Ni₃Ti) could be significantly reduced by adjusting the partial pressure of the reactant gases. This shows that CVD of TiN on cutting tools with Fe or Ni as a binder phase needs to be optimized with respect to the process parameters.

Thermodynamic calculations of the Ti(C,N) CVD process indicates that the major growth species using CH₃CN, TiCl₄ and H₂ as precursors, was HCN and TiCl₃. They were formed in the gas phase by homogeneous reactions. Furthermore, it was found that by adjusting the composition of the reaction gas mixture, the preferred orientation, morphology, and microstructure of the Ti(C,N) coatings could be tailored. As a result, the tribological/mechanical properties of the Ti(C,N) coatings could be significantly improved. A hardness of 40 GPa, i.e. close to super hard could for instance be achieved. The origin of the mechanical improvements was attributed to a more ordered crystallographic orientation in the <111> direction as well as a high defect density close to the coating surface. In addition to the excellent mechanical properties, the Ti(C,N) coatings were also found to have a high corrosion resistance in sea water, thanks to a formation of a passivating surface layer (TiO₂).

Keywords: CVD, Hard coatings, Ti(C, N), TiN

Linus von Fieandt, Department of Chemistry - Ångström, Inorganic Chemistry, Box 538, Uppsala University, SE-751 21 Uppsala, Sweden.

© Linus von Fieandt 2018

ISSN 1651-6214

ISBN 978-91-513-0184-6

urn:nbn:se:uu:diva-335907 (<http://urn.kb.se/resolve?urn=urn:nbn:se:uu:diva-335907>)

List of Papers

This thesis is based on the following papers, which are referred to in the text by their Roman numerals.

- I von Fieandt, L. Larsson, T. Lindahl, E. Bäcke, O. Boman, M. (2018) Chemical vapor deposition of TiN on transition metal substrates. *Surface & Coatings Technology*, 334C:373-373.
- II von Fieandt, L. Larsson, T. Boman, M. Lindahl, E. (2017) Texture formation in chemical vapor deposition of Ti(C,N). *In manuscript*
- III von Fieandt, L. Johansson, K. Larsson, T. Boman, M. Lindahl, E. (2018) On the growth, orientation and hardness of chemical vapor deposited Ti(C,N). *Thin Solid Films*, 645:19-26
- IV von Fieandt, L. E. Bäcke, O. Larsson, T. Lindahl, Boman, M. (2017) Deformation behavior of highly oriented Ti(C,N) *In manuscript*.
- V von Fieandt, L. Fallqvist, M. Larsson, T. Lindahl, E., Boman, M. (2018) Tribological properties of highly oriented Ti(C,N) deposited by chemical vapor deposition. *Tribology International*, 119:593-599.
- VI von Fieandt, L. Johansson, K. Larsson, T. Boman, M. Lindahl, E. Rehnlund, D. (2017) Corrosion properties of CVD grown Ti(C,N) coatings in artificial seawater environments. *Submitted*.

Reprints were made with permission from the respective publishers.

My contributions to the publications

- I. Planned the experiments, performed all the analyses except the TEM investigation in which I took part. Wrote the manuscript (main author)
- II. Planned the experiments, performed all the analyses and wrote the manuscript (main author).
- III. Took part in the experiment planning, performed all analyses except the XPS part, wrote the manuscript (main author).
- IV. Planned the study, performed the nanoindentations and parts of the TEM sample preparations and wrote the manuscript (main author).
- V. Took part in the planning, took part in the tribological testing, performed all analyses and wrote the manuscript (main author).
- VI. Took part in the planning, performed AFM and SEM analyses, took part in writing the manuscript.

Contents

1. Introduction.....	9
Scope of this thesis.....	11
2. Deposition and thermodynamic calculations	12
2.1. Chemical vapor deposition	12
2.2. Coating materials.....	15
2.2.1. Titanium nitride	15
2.2.2. Titanium carbonitride	16
2.3. Wear mechanisms	17
2.4. Thermodynamic calculations	17
3. Characterization	19
3.1 X-ray diffraction (XRD).....	19
3.2. Scanning electron microscopy (SEM).....	21
3.2.1. Energy dispersive X-ray spectroscopy (EDS)	21
3.2.2. Electron backscatter diffraction (EBSD)/Transmission Kikuchi diffraction (TKD).....	21
3.3. Transmission electron microscopy (TEM).....	22
3.3.1. Bright field (BF)	22
3.3.2. Dark field (DF)	22
3.3.3. High angle annular dark field (HAADF).....	22
3.4. Focused ion beam (FIB).....	23
3.5. Atomic force microscopy (AFM).....	23
3.6. X-ray photoelectron spectroscopy (XPS).....	23
3.7. Mechanical properties	24
3.7.1. Nanoindentation.....	24
3.7.2. Microabrasion	24
3.7.3. Scratch testing.....	25
3.8 Corrosion resistance	25
4. Results and discussion	27
4.1 TiN deposition on d-metal substrates	27
4.2. Kinetics and growth of Ti(C,N)	34
4.2.1. TiCl ₄ and CH ₃ CN series	35
4.2.2. Nitrogen modified Ti(C,N) deposition.....	37

4.3. Orientation, microstructure and morphology of Ti(C,N) and its implications on the mechanical properties	41
4.3.1. Morphology and microstructure of Ti(C,N)	41
4.3.2. Orientation	43
4.3.3. Texture forming mechanism in Ti(C,N) deposition	45
4.3.4. Implications of the orientation and microstructure on the Ti(C,N) hardness	47
4.3.5. Hardening mechanism	49
4.4. Tribology of Ti(C,N).....	55
4.4.1. Microabrasion tests.....	56
4.4.2. Scratch tests	57
4.5. Corrosion resistance of Ti(C,N)	60
5. Concluding remarks	65
6. Sammanfattning på svenska.....	67
7. Acknowledgements.....	71
8. References.....	72

Abbreviations

AFM	Atomic force microscopy
CVD	Chemical vapor deposition
CCP	Cubic close packing
EBSD	Electron backscatter diffraction
EDS	Energy dispersive X-ray spectroscopy
ESCA	Electron spectroscopy for chemical analysis
FWHM	Full width at half maximum
HSS	High speed steel
PVD	Physical vapor deposition
SEM	Scanning electron microscopy
TKD	Transmission Kikuchi diffraction
TEM	Transmission electron microscopy
XPS	X-ray photoelectron spectroscopy

1. Introduction

Mankind has been using tools in order to aid collection of natural resources for more than 2 million years, and the first rudimentary tools were made of rocks and sticks [1]. Evolution has taken us many steps since then to complex alloys engineered down to the atomic level [2]. The more sophisticated materials we have invented, the more sophisticated tools are needed to manufacture and process them.

The development of modern cutting tools started with the use of carbon steels, which were introduced in the 19th century, and later on high-speed steels (HSS) were introduced in the early 20th century. Especially the invention of HSS led to a significant reduction of machining times, which was attributed to the high hot hardness [3]. The next leap forward in the evolution from high speed steels was tools consisting of a tungsten carbide hard phase sintered in a cobalt binder/matrix. This composite material, also called hard metal or cemented carbide, was invented during the First World War due to a shortage of regular tool material. The first patent on hard metal was registered in 1923, and thereafter the use of hard metal spread. The first Swedish hard metal producer was Fagersta Bruks AB, which started its production in 1931 [4].

The next revolution in the tooling world was the use of a thin surface coating of TiC on the hard metal tool. This coating was deposited using chemical vapor deposition (CVD), and led to a revolutionizing increase in the tool life, between 2 and 10 times better compared to for the uncoated tools [5,6]. The high hot hardness, excellent diffusion barrier properties and good tensile strength of the coating yielded an improved tool life despite the fact that the coating was only a few microns thick.

Since the introduction of the TiC coating, several other coatings have been developed, e.g. TiN, Ti(C,N), TiAlN, Al₂O₃, and combinations of these are a few examples of coatings used in the industry today [7–12]. In the late 1980s an additional coating technique was introduced in the cutting tool industry, physical vapor deposition (PVD). The introduction of PVD enabled deposition at lower temperatures, compared to CVD, and therefore the use of more sensitive substrates [5,7,13].

This thesis is focused on how to improve many properties of the CVD coatings used in the cemented carbide industry today, such as hardness, adhesion and crack resistance as well as corrosion resistance. Several approaches have been suggested to achieve these improvements, i.e. tuning of

crystallographic orientation, tuning the composition of the coating and applying multi-layers of several different coating materials [9,14–19]. The investigations in this thesis have focused on improving and investigating the CVD processes used to manufacture TiN and Ti(C,N) coatings.

Scope of this thesis

The aim of this thesis is to investigate the growth behavior of CVD deposited Ti-based hard coatings and to increase the understanding of how the properties of the coatings can be controlled by the deposition process, thereby increasing the mechanical performance of the coatings. This aim is approached via the following steps:

- Investigation and optimization of the growth of TiN on different metallic substrates suited as binder phase in cemented carbide.
- Investigation of the growth mechanism of Ti(C,N) deposition from TiCl₄ and CH₃CN.
- Optimization of texture and microstructure of Ti(C,N) with regards to mechanical properties.
- Investigation of tribological properties of Ti(C,N) coatings with different microstructures and orientations.

2. Deposition and thermodynamic calculations

2.1. Chemical vapor deposition

The high melting point of the coatings used in cutting applications (typically ~3000 °C) makes them rather impractical to synthesize through bulk methods [20–22]. At such high temperatures the substrate material (WC-Co) is affected in a negative way, e.g. via melting of the Co-binder and undesirable grain growth of the WC phase. It is therefore better to deposit the coatings by a thin film deposition method, such as CVD or PVD, where much lower temperatures typically are needed.

All coatings in this thesis were deposited using CVD. This deposition technique uses a continuously flowing gas phase, from which the solid films are deposited on a substrate surface. It is typically carried out at a low pressure (below 10 kPa) to enable the use of volatile/air sensitive reactants. Two different kinds of reactions can occur: homogenous reactions in the gas phase, and heterogeneous reactions on the surface of the substrate. The heterogeneous reactions are the ones forming the desired solid film [23].

Reactions forming solid products in the gas phase (homogeneous nucleation) are generally unwanted, as the solid will fall down on the substrates as particles, yielding poor adhesion or unwanted inclusions in the coating. This can be avoided by choosing reactants that need a thermal activation, i.e., the CVD reaction needs to be thermally activated and will not proceed at room temperature. There are several other approaches to activate the reaction gas mixture. Heating by a laser pulse (LA-CVD), degrading molecules by UV light (UV-CVD), activation in a plasma (PA-CVD) are just a few examples of such processes. Thermal activation, was the only approach used in this thesis [24,25].

There are three possible modes of thermal CVD: hot wall CVD in which the entire reaction chamber is heated, cold wall CVD where only the substrates are heated, and hot filament CVD where the gas is activated by a filament [23,26]. The depositions in this thesis were carried out using hot wall CVD, a technique well suited for mass production by batch processing as many substrates can be coated simultaneously.

The film forming reactions, or the mechanisms, in CVD are generally rather complex as they typically involve many elementary steps such as: homogeneous reactions in the gas phase (preferably not resulting in a solid phase), adsorption on the substrate surface, surface reactions, and desorption

from the surface. If the rate-limiting step involves reactions on the surface, the process is surface kinetically controlled. A coating process under surface kinetics control will yield coatings of an even thickness throughout the entire reactor because of the high step coverage.

The reaction rate or the deposition rate of the CVD process under surface kinetics control will increase exponentially with an increased reaction temperature up to the point where the reactions are depleting the gas phase faster than new precursors can be supplied. The reaction is then said to be under mass transport control (or only transport controlled), where the reaction rate is determined by the diffusion rate of the precursors towards the surface of the coating. A process under mass transport control has much lower step coverage and this can lead to a non-uniform coating thickness in the reactor, as the gas phase will be consumed prior to reaching the periphery of the reactor.

The mode of the reaction can be deduced by making an Arrhenius plot, in which the logarithm of the reaction rate is plotted against the reciprocal reaction temperature [26]. The slope of the line in the Arrhenius plot then represents the apparent activation energy of the reaction. A slope with a high negative value in the range of 100-300 kJ/mol often indicates a reaction under surface kinetics control [26]. The slope in the mass transport limited region can either be positive, for exothermic processes, or negative, for endothermic processes, and are typically lower value than for a reaction in kinetic control [26]. Furthermore, to determine the reaction order of a certain reactant under kinetic control a log-log plot can be made in which the growth rate is plotted versus the reactant partial pressure. The slope of the line gives the reaction order of the investigated reaction.

In this thesis, industrial large-scale hot-wall CVD reactors have been used for coating deposition. A schematic illustration of the reactors used is shown in **Figure 1**. The reactor is constructed in such a way that the gas is introduced at the bottom of the reactor and then distributed over the substrates via a rotating gas distribution tube. The reactor is heated by a resistively heated external furnace surrounding the reactor.

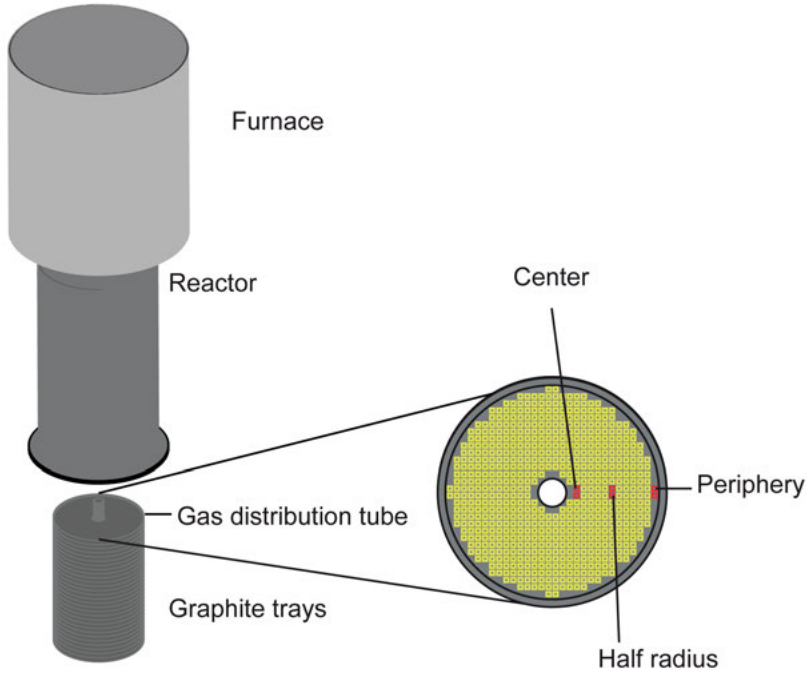
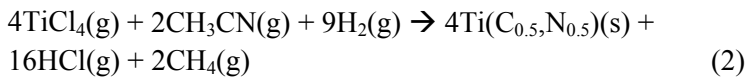
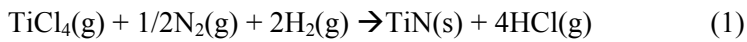


Figure 1. Reactor schematics and overview of the sample and control piece positions.

The TiN and Ti(C,N) coatings in this thesis were deposited using thermal CVD. The simplified overall deposition reactions, for TiN and Ti(C,N) respectively, are as follows:



The reactions presented above are overall reactions and give no details about side reactions or the mechanisms (elementary steps) involved in the gas phase and on the surface of the substrates.

2.2. Coating materials

The conditions in cutting applications are in most cases considered quite extreme, with temperatures sometimes exceeding 1000 °C and local pressures in the GPa range. Such conditions put extraordinary demands on the coating materials, regarding: high hot hardness, chemical inertness towards the work material and good adhesion to the substrate. To be able to meet all these demands a CVD coated metal cutting tool is often composed of several different coating layers. Starting with a TiN layer closest to the substrate, followed by layers of Ti(C,N) and Al₂O₃. In this thesis, the focus has been on the initial TiN layer and the next Ti(C,N) layer.

2.2.1. Titanium nitride

Titanium nitride is used in metal cutting due to its relatively high hardness and chemical inertness. In addition to its use in the tooling industry, TiN has also been used in several other fields, e.g. as diffusion barriers in the semiconductor industry and for corrosion protection of stainless steel [27,28].

The relatively high hardness and melting point of TiN, about 20 GPa and 2950 °C respectively, make it suitable for use in abrasive operations at high temperatures, such as in a cutting operation [29]. Titanium nitride is normally the first layer deposited on a cutting tool made of cemented carbide, where the TiN is used as a nucleation layer for the succeeding Ti(C,N) layer. It has been shown that the adhesion between the tool and the Ti(C,N) layer can be improved substantially by depositing a TiN layer on the cemented carbide tool prior to deposition of Ti(C,N) [30,31]. The improved adhesion was believed to be caused by diffusion of W, Co and C from the substrate into the TiN layer.

As TiN is commonly the first layer to be deposited on a cutting tool, the gas phase, from which TiN is deposited, may interact with the surface of the tool. Since the reaction gas mixture is corrosive, it is important to use an inert composition of the cemented carbide. WC and Co are such inert compositions and have worked for many years. Recent trends in WC-Co manufacturing points towards replacing Co as a binder phase metal due to health concerns [32,33]. However, it has been shown that a change of binder metal to other suitable candidates, e.g. Ni or Fe, affects the deposition process and the resulting coating with respect to deposition rate, coating morphology and coating adhesion [34–39]. It was shown that deposition of TiN on Ni-containing substrates were especially problematic, yielding a coating composed of several phases rather than the desired single phase TiN [38,39]. The problems were attributed to the formation of NiCl₂ through etching of the substrate. Similar problems are expected to occur if the binder phase is Fe based, as etching of the substrate through formation of iron chlorides most likely will take place, thus forming a poor coating – tool interface [40].

There are several precursors available for CVD of TiN, however the reaction between TiCl_4 , H_2 and N_2 is commonly used in the tooling industry. This reaction usually takes place above $800\text{ }^\circ\text{C}$ and at pressures between 1 kPa and atmospheric pressure [7,24]. Another common reaction for TiN deposition is the reaction between NH_3 and TiCl_4 at temperatures as low as $400\text{ }^\circ\text{C}$. In this case the pressure needs to be kept low, usually below 1 kPa, and/or the reactants separated until they reach the substrate in order to prevent homogeneous reactions in the gas phase [7,24].

2.2.2. Titanium carbonitride

Apart from its use in the tooling industry, several other fields are making use of the interesting properties of $\text{Ti}(\text{C},\text{N})$. For example, the biocompatibility and the nontoxic nature of $\text{Ti}(\text{C},\text{N})$ make it excellent for biomedical applications [41,42]. Furthermore, $\text{Ti}(\text{C},\text{N})$ has shown great promise as a corrosion protective coating in harsh environments [43].

$\text{Ti}(\text{C},\text{N})$ is a solid solution of TiC and TiN, in which the properties of both materials are retained, i.e. the high hardness of TiC, about 28 GPa, and chemical inertness of the TiN. TiC and TiN both have a NaCl type structure and are fully miscible, thus enabling a variation of the composition between 100% carbide and 100% nitride [44].

The mechanical properties of deposited $\text{Ti}(\text{C},\text{N})$ can be varied through changes in the composition, e.g. the hardness can be improved by increasing the C/N ratio [16,17]. The composition and texture, i.e. the preferred orientation of the crystallites of the deposited coating are largely influenced by the choice of precursors and process parameters, such as temperature and pressure [14–17]. Two different deposition reactions are typically used to deposit $\text{Ti}(\text{C},\text{N})$: the moderate temperature (MT) process at $750\text{--}900\text{ }^\circ\text{C}$, and the high temperature (HT) process above $900\text{ }^\circ\text{C}$. The two different processes use different C and N precursors while TiCl_4 is used as a Ti source in both processes. The MT process uses CH_3CN as a single-source precursor for both carbon and nitrogen. The HT process uses CH_4 and N_2 as the carbon and nitrogen precursors, respectively. Both processes typically operate at pressures below 8 kPa.

CH_3CN is more reactive than CH_4 and N_2 , thus enabling higher deposition rates at lower temperatures [12,45]. Furthermore, the composition of coatings deposited using the MT-process have been found to be on the carbon-rich side and sub stoichiometric on C and N and are typically deposited as $\text{Ti}(\text{C}_{0.6},\text{N}_{0.4})_{0.8}$ [46]. Coatings deposited on WC-Co tools using the MT-process have been found to exhibit a $\langle 211 \rangle$ preferred growth orientation. These coatings grow in a columnar fashion and have grains with a ridge-like surface morphology, where the grains are twinned on a $\{111\}$ plane [46].

The compositions of coatings deposited using the HT process are more dependent on the flow rates of the different precursors, CH_4 and N_2 , and the

temperature during the deposition [14–17]. It has also been shown that the preferred orientation and grain morphology of these coatings differ significantly depending on precursor flow rate and deposition temperature [14,15].

2.3. Wear mechanisms

Despite both the substrate and coating material being significantly harder and more chemically inert than the workpiece material they still undergo extensive wear. Several different wear mechanisms are possible in a metal cutting process, e.g. chemical wear, abrasive wear, and adhesive wear. Chemical wear is caused by high temperatures induced in the cutting process, which causes the material of the tool to react chemically with the chip of the work piece material. Abrasive wear is caused by hard inclusions, typically oxide particles, in the work piece material which act as abrasives on the tool. Adhesive wear is caused by adhesion between the chip and the tool surface, leading to a buildup that subsequently is torn away, taking with it parts of the tool surface. Development of coatings and WC-Co tools aim to reduce the wear and thus to increase the life time of the tools [47].

2.4. Thermodynamic calculations

As mentioned above, the reactions in a CVD process are often complex and involving several reaction steps and surface interactions. Given the complexity of the involved reactions, theoretical calculations are often good tools to gain a deeper understanding of the process. The reactions in the gas phase and the interactions between the gas phase and the substrate can be modelled through thermodynamic equilibrium calculations. Several key insights can be gained from such calculations: e.g. regarding the composition of the gas mixture, interactions between the gas phase and substrate and which species that are important for the coating growth. However, the thermodynamic calculations give no information about reaction kinetics. Anyhow, reactions having reasonable fast kinetics are usually modelled well by thermodynamics. If thermodynamic calculations are combined with kinetic calculations and/or kinetic experimental data, a better understanding of the CVD process is usually achieved.

In this thesis a free-energy minimization technique was used to model the conditions during the CVD growth. In paper **I**, the interactions between the gas phase and the substrate were modeled in order to determine substrate reactivity towards the gas phase. In paper **III**, the main growth species were determined using thermodynamic calculations.

The EkviCalc software by BeN systems was used for all the thermodynamic calculations in this thesis [48].

3. Characterization

Several different characterization techniques were employed to characterize the coatings deposited in this thesis. A description of the used techniques is presented in the following section.

3.1 X-ray diffraction (XRD)

XRD is a well-known technique based on constructive or destructive interference of a coherent X-ray beam impinged on the sample. The result of the measurement is a diffraction pattern from which several things can be deduced. The crystal structure, lattice parameters and the orientation of the crystallites are some examples of information that can be extracted from a diffraction pattern.

In this thesis four different diffraction techniques have been utilized: θ - 2θ diffraction, grazing incidence (GI)-XRD, rocking curve measurements (ω – scans) and pole figure measurements. In θ - 2θ diffraction the incoming beam and the detector are scanned symmetrically, i.e. the angle of the detector relative to the substrate surface is kept at two times the incident angle (θ/ω , see **Figure 3**). In this measurement only crystal planes in parallel with the sample surface will be measured why out of plane orientation can be decided as well as inter- planar distances in the crystal.

This scan method is not optimal for thin films as the volume of the thin film probed by the X-ray beam decreases as the incidence angle of the beam is increased, causing the diffracted beam intensity to drop, see **Figure 2b**.

To increase the probability of diffraction from a thin film, where the probed volume is typically small, GI-XRD can be used. In GI-XRD, the incident beam is kept at a constant angle (typically 0.5 - 3°) and the detector is scanned in 2θ . The probed volume of the film is then increased, thus increasing the intensity of the diffracted signal from the film, see **Figure 2a**. A GI-XRD measurement probes planes with several spatial orientations, i.e. not only planes parallel to the surface. Therefore, the preferred orientation of the film is not easily obtained from a GI-XRD scan. Furthermore, thin films often exhibit a preferred out-of-plane orientation (texture) which causes the peak intensities to deviate from what could be expected from a randomly oriented sample (powder). This causes problems in phase determination as several peaks could be completely absent in a highly textured sample.

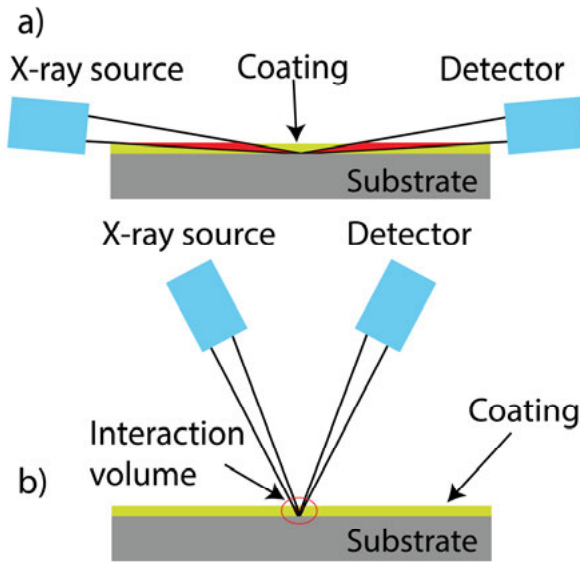


Figure 2. Interaction volume of X-rays with thin film indicated in red, for a) low incidence angle, and b) high incidence angle.

In a rocking curve measurement (ω -scan) the detector is kept at a fixed position, i.e. at a fixed 2θ , and the sample is scanned in ω . In this scan type the degree of orientation of the crystallites in the coating can be investigated. A perfect single crystalline sample would produce a peak with a width corresponding to the resolution of the instrument while a random oriented sample (powder) would yield in no peaks at all [49]. A schematic illustration of the axes and angles used in the diffraction measurements is shown in **Figure 3**.

A pole figure measurement can be used to determine the orientation of the crystallites both out-of-plane and in the sample surface plane (in-plane). In a pole figure measurement the 2θ angle is kept constant at a suitable diffraction peak i.e. a pre-selected $\{hkl\}$ is measured. The sample is then stepwise tilted in Ψ between 0 and 90 ° and for each such tilt a complete 360° Φ scan is made. The measurement will measure the angular distribution of the chosen $\{hkl\}$ planes in the sample as a function of Phi and Psi in that way both in-plane and out of plane orientations are determined [49]. If the coating has order in-plane, i.e. the crystallites are aligned in the substrate plane, there will be discrete spots in the pole figure (epitaxy). If there is no in-plane ordering, a ring will appear instead, indicating a free rotation in plane. The coating then has a fiber texture.

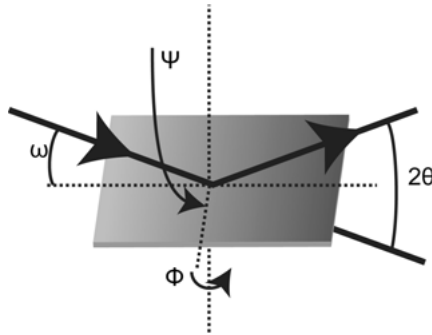


Figure 3. Schematic illustration of the angles/axis used in the diffraction measurements

3.2. Scanning electron microscopy (SEM)

The coating thickness, cross-section microstructure, top view grain morphology, elemental composition, phase composition, and orientation have been investigated using a scanning electron microscope. In contrast to a conventional optical microscope, a SEM uses electrons instead of visible light. The use of electrons enables much higher resolution than with optical microscopes due to the shorter wavelengths of the electrons compared to for visible light [50].

Electrons interact strongly with matter, which is utilized in the SEM in several ways. Secondary electrons can be ejected from the illuminated sample, these electrons are then collected by a secondary electron detector and used for imaging of the sample.

3.2.1. Energy dispersive X-ray spectroscopy (EDS)

Electron – matter interactions can also cause X-ray emission, upon illumination an elemental characteristic X-ray can hence be emitted from the sample [50]. Emitted X-rays can be collected by a detector (energy dispersive or wavelength dispersive) and analyzed to enable elemental mapping. In this thesis an energy dispersive detector has been used.

3.2.2. Electron backscatter diffraction (EBSD)/Transmission Kikuchi diffraction (TKD)

Diffraction can also occur when electrons interact with a crystalline sample, as electrons from the incident beam are scattered by the sample crystallites.

The scattering can either be in the back-scatter mode for a thick sample (>200nm) or in the transmission mode for samples thinner than 200 nm. The scattered electrons can form a Kikuchi pattern, from which the orientation and phase content of the analyzed area can be determined [51].

The strong interactions between electrons and matter make it necessary for an SEM to operate in vacuum in order to minimize the interactions between electrons and air.

The microscope used in this thesis was a Zeiss Merlin High resolution SEM equipped with an X-max 80mm² silicon drift EDS detector and an Oxford Nordlys EBSD detector.

3.3. Transmission electron microscopy (TEM)

The TEM also utilizes electrons as the light source, however, in the TEM the electrons are transmitted through the sample instead of reflected as in the SEM case. As mentioned above, electrons interact strongly with the sample, thereby a thin sample (≤ 200 nm) is required. A TEM can be operated in the scanning mode (STEM), where the electron beam is converged in to a small (sub Å) probe or in the conventional TEM mode where the beam is parallel. Depending on which information one wants to extract from the sample different detectors are available. Two different microscopes were used in this work: a FEI Themis and a FEI Titan 80-300.

3.3.1. Bright field (BF)

Areas with low density, low thickness, low atomic number (Z), or low crystallinity will appear bright in this mode, in which the electrons scattered close to the optical axis are collected [50,51]. There are BF detectors both for the conventional and scanning modes.

3.3.2. Dark field (DF)

Quite intuitively DF is the opposite of BF, where electrons scattered further away from the optical axis are collected. Thus, areas with high Z as well as highly crystalline areas will appear bright [50,51].

3.3.3. High angle annular dark field (HAADF)

The HAADF detector is placed sufficiently far away from the optical axis to avoid collection of diffracted electrons, thus giving rise to a Z -contrast image [51]. A proper setup of the microscope and a sufficiently thin sample can yield HAADF images with atomic resolution. The preferred orientation of the crystallite can be obtained by either convergent beam diffraction (CBED)

or by the fast Fourier transform (FFT) of the high resolution (HR) image. This detector operates in the STEM configuration of the microscope.

3.4. Focused ion beam (FIB)

A FIB instrument uses ions for imaging rather than electrons. Combinations of both electrons and ions are also common (dual beam instruments). An advantage of using ions compared to electrons is the possibility to etch the sample on the micro/nano scale. As an impinging ion has a many times higher mass than an electron material from the sample will be knocked out, thus enabling etching with very high lateral resolution.

FIB milling was used to manufacture thin lamellas for TKD/TEM measurements following the procedure described in [52,53].

A FEI Strata DB235 and a FEI LoVac DualBeam FIB were used for the production of TKD/TEM lamellas in this thesis.

3.5. Atomic force microscopy (AFM)

Surface roughness and morphology can be studied using AFM. A sharp (atomically) Si-tip mounted on a cantilever beam is scanned over a sample surface and the atomic interactions between the tip and the surface causes a deflection of the cantilever beam. The deflection of the beam is measured by the deflection of a laser beam. In this way very high spatial resolution can be achieved (atomic under optimal conditions) and the surface can be mapped in three dimensions [54]. In this thesis a PSIA XE150 AFM has been used. All the measurements were made in the non-contact mode.

3.6. X-ray photoelectron spectroscopy (XPS)

XPS is a technique that uses X-rays to probe the surface of a material. There are several possible events that can occur when a material is probed by X-rays. As mentioned earlier diffraction can occur. Another possibility is the excitation of the material and subsequent ejection of a photoelectron. The kinetic energy of the ejected photoelectron is measured and the electron binding energy can be calculated. This binding energy is specific for each element, which enables elemental identification by XPS. Furthermore, the binding energies are affected by the chemical environment of the element. This enables chemical analysis by XPS [55]. As mentioned earlier, electrons have a strong interaction with matter, so only the electrons emitted close to the surface (a few nm) have a preserved kinetic energy. This makes XPS a highly surface sensitive technique. Although surface sensitive, depth profiles

can be obtained through sequential sputtering. The high surface sensitivity requires UHV conditions in the measurement chamber in order to avoid surface oxide buildup and collisions between photoelectrons and ambient gas molecules. In this thesis two different instruments have been used: a Physical Electronics Quantum 2000 scanning Electron Spectroscopy for Chemical Analysis (ESCA) microprobe, and a Physical Electronics Quantera II scanning ESCA microprobe. Both instruments used monochromatic Al-K α radiation.

3.7. Mechanical properties

Coatings that are intended for use in cutting applications needs to have outstanding mechanical properties such as hardness and adhesion. To increase the understanding of how material properties such as preferred orientation, morphology and microstructure affect the mechanical properties lab scale tests can be employed to isolate each property under controlled conditions.

3.7.1. Nanoindentation

Nanoindentation can be used to determine the hardness and Young's modulus of a thin film without influence from the substrate. This method includes pressing a diamond indenter into the selected material while measuring the impression depth as a function of the applied force. The hardness of the coating is given as a ratio of the maximum load and the load carrying area. By measuring the slope of the unloading curve the Young's modulus can be obtained. Both the hardness and Young's modulus were calculated according to the method by Oliver and Pharr [56]. A CSM UNHT nanoindenter with a Berkowich diamond indenter was used for the hardness measurements.

3.7.2. Microabrasion

Resistance to abrasive wear is an important property of any coating used in metal cutting. In order to evaluate the abrasive wear resistance microabrasion tests have been used. This test uses a dimple grinder (typically used for mechanical TEM sample preparation) with a wheel of stainless steel. The wheel is soaked in abrasive slurry, in this thesis a diamond slurry was used. A load is applied to the wheel and as a result a crater will be made in the sample. The abrasive wear rate (κ) can be calculated by measuring the volume of the crater (V_g) and then employing the following equations [57]:

$$V_g \approx \frac{\pi b^4}{64R} \quad (\text{for } b \ll R) \quad (1)$$

$$SL = \frac{V_g}{\kappa} \quad (2)$$

Where b is the outer diameter of the crater, R is the radius of the wheel, S is the sliding distance of the wheel and L is the normal load.

In this thesis a Gatan 656 dimple grinder with a stainless steel wheel ($r = 10$ mm) with a constant load of 0,2 N and a rotation speed of 100 rpm was used. The diamond slurries used consisted of 1 and 6 μm diamond particles respectively (Kemet® Liquid diamond Type WX XStr).

3.7.3. Scratch testing

Apart from a coating's resistance to mechanical wear, the life time of the tool in a cutting operation is strongly dependent on the adhesion between the coating and the tool. Poor adhesion between the tool and the coating is detrimental for the tool life. Scratch testing is the most common method to evaluate the tool-coating adhesion (also coating – coating adhesion in the case of multilayers) [58–61]. The most common setup in scratch testing uses a conical indenter (Rockwell C) with a diamond tip of 200 μm radius. Applying the indenter under a controlled load (increasing or constant) gives a response from the coating from which the failure mechanisms of the coating can be determined. The failure of the coating is coupled to the applied load, as the initial cracking occurs at the first critical load (L_{c1}) whereas continuous coating delamination/spalling occurs at the second critical load (L_{c2}). An Anton Paar Revetest scratch rig was used for the scratch tests.

3.8 Corrosion resistance

Protective coatings can also be used to enhance the corrosion resistance of a surface. Surface corrosion is a common problem for many metals and alloys used in marine applications. TiC and TiN coatings have shown promising corrosion protection properties in previous studies, however few studies has been made on Ti(C,N) [12,62–67]. It was therefore interesting to investigate the corrosion properties of Ti(C,N) in more detail.

The corrosion resistance of Ti(C,N) was investigated in paper VI using potentiodynamic polarization measurements, in which the electrical potential was scanned from a negative potential, - 1.5 V (reducing potential) to a positive potential 1.5 V (oxidizing potential) in a stepwise manner. The resulting current response then showed regions of oxidation and passivation of the probed surface. The corrosion measurements were carried out in an artificial seawater environment (3.5 wt % NaCl aqueous electrolyte). A VersaSTAT4 (Princeton Applied Research) potentiostat/galvanostat was used for the

measurements. The sample surface (Ti(C,N)) was used as the working electrode while a Pt wire was used as counter electrode and a saturated Ag/AgCl electrode was used as the reference electrode.

4. Results and discussion

4.1 TiN deposition on d-metal substrates

The first coating layer commonly deposited on WC-Co cutting tools is TiN, as it serves to improve the adhesion to the following layers [30,31]. In paper I it was found that the nucleation and growth behavior of TiN is strongly dependent on the substrate used. There are several important aspects to consider, e.g. the catalytic activity of the substrate which may influence the dissociation of the molecules in the gas phase and the inertness of the substrate towards the gas phase. Reactions between the substrate and the gas phase are generally undesired as etching of the substrate can cause corrosion thereby generating poor substrate/coating interfaces. Etching of the substrate can be caused by either HCl formed when TiCl_4 is reduced by H_2 in the gas phase or by substrate-assisted reduction of titanium chlorides. The latter mechanism is more likely when a reactive metal is used as a substrate, e.g. a Fe substrate where FeCl_x can form from the titanium chlorides in the gas phase. Furthermore, gaseous substrate chlorides that can be reduced by the H_2 in the gas phase, can be incorporated as metal in the growing coating (auto doping), see *Figure 4*.

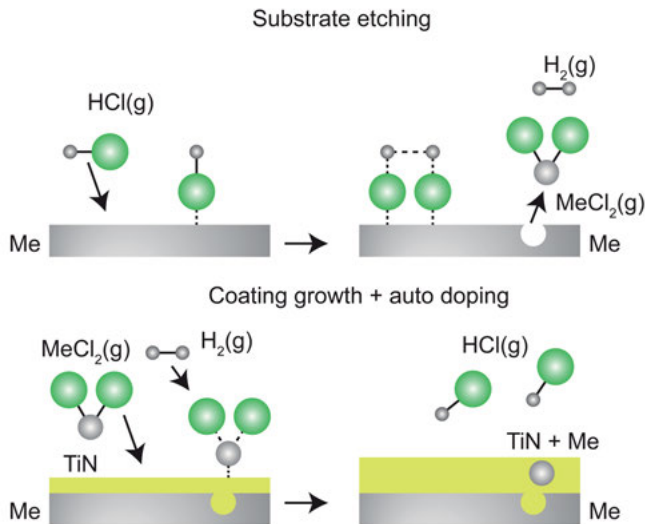


Figure 4. Schematic view of substrate etching and auto doping during TiN deposition, by chlorides in the gas phase (HCl in this case).

TiN was deposited on three different d-metal substrates in order to study their reactivity during the CVD of TiN. Co, Fe and Ni substrates were chosen, all of which are suitable for use as the binder phase in cemented carbides. The interactions between the reaction gas mixture and the substrates were investigated by thermodynamic calculations and experimentally in the temperature 850-950 °C range. Detailed experimental parameters can be found in the experimental section of paper I.

Thermodynamic calculations predicted that the formation of metal chlorides (etching) will be most prominent when Fe substrates are used, see **Figure 5**. The thermodynamic calculations also predicted that a Ni substrate would be the most inert toward the gas phase of the investigated metals.

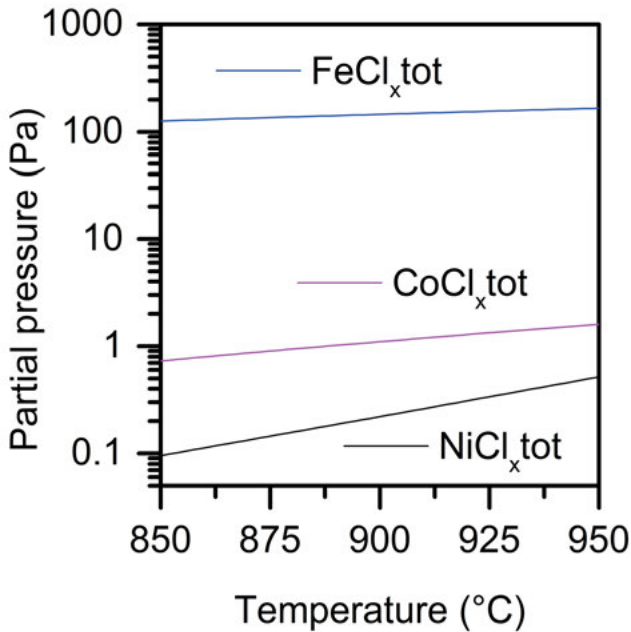


Figure 5. Partial pressure of metal chlorides in the gas phase after TiN deposition. $FeCl_x tot = FeCl_2 + Fe_2Cl_4 + FeCl_3 + FeCl + Fe_2Cl_6$. $CoCl_x tot = CoCl_2 + CoCl + Co_2Cl_4 + CoCl_3$. $NiCl_x tot = NiCl + NiCl_2$.

The thermodynamic calculations also predicted that there might be a different growth behavior on Fe substrates compared to on Ni and Co since Fe is less inert than Co and Ni.

The deposited coatings were examined by GI-XRD, where it was found that TiN was indeed deposited on Co, Fe, and Ni substrates, see **Figure 6**. However, TiN deposited on Ni substrates also featured an additional phase, Ni₃Ti, see **Figure 6c**. No other phases, including etching products, were identified in any of the deposits.

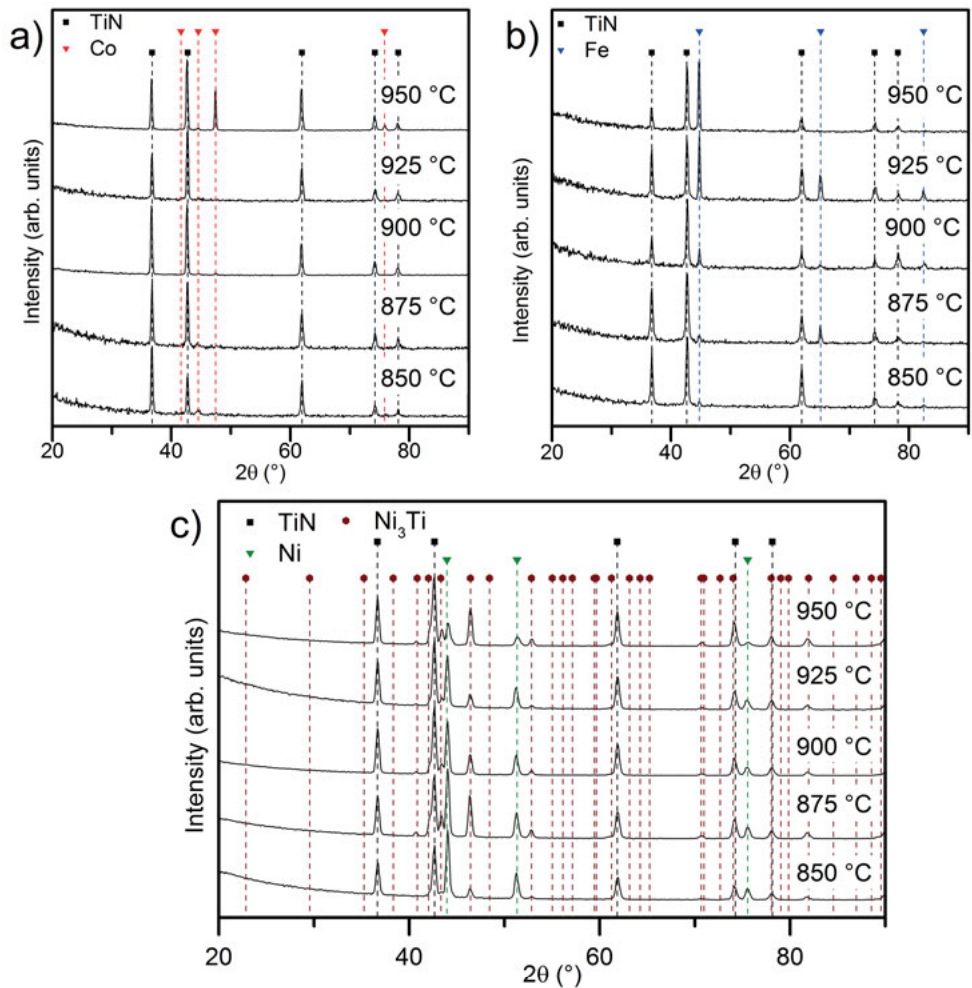


Figure 6. GI-XRD diffractograms of TiN deposited on: a) Co, b) Fe, c) Ni.

Typical morphologies and microstructures of TiN deposited on the three substrates are shown in **Figure 7**.

TiN deposited on Co substrates exhibited a mixture of grain morphologies, consisting mainly of ridge-like grains and smaller amounts of star-shaped grains as well as needle-like grains, see **Figure 7a**. All the deposited coatings had a dense columnar microstructure, **Figure 7d**. These observations were in agreement with previous studies of TiN deposited on WC-Co substrates [68].

TiN deposited on Fe substrates had a morphology different to that of TiN on Co substrates, see **Figure 7b**. The grain morphology was a mixture of mainly standing platelets and a small amount of star shaped grains as well as areas of small needle like grains. This indicates that there is a difference in the kinetics for the deposition on Fe compared to on Co substrates, where a

completely different morphology was obtained. Furthermore, the cross sections of the TiN deposited on Fe showed that severe corrosion of the substrate had occurred, **Figure 7e**.

TiN deposited on Ni substrates had morphologies featuring nodular grains, differing from both Fe and Co, **Figure 7c**. The cross section of the TiN deposited on Ni revealed an inhomogeneous and porous microstructure, **Figure 7f**. The interface consisted of areas having two different contrast levels, indicating that two or more phases had formed.

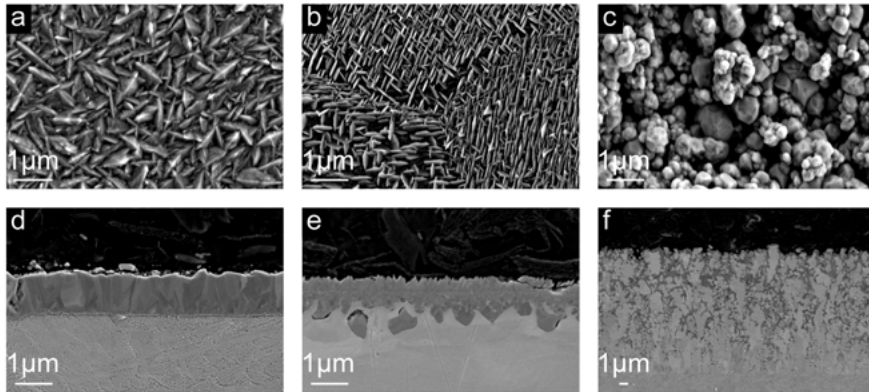


Figure 7. SEM top view micrographs of TiN deposited on a) Co, b) Fe, c) Ni. Cross section micrographs of TiN deposited on d) Co, e) Fe, f) Ni.

A TEM lamella was made of the sample deposited at 950 °C on Ni in order to identify the phases. **Figure 8** shows the TKD analysis of the lamella, where it can be seen that three different phases were present, Osbornite (TiN), Ni₃Ti and metallic Ni. This is in good agreement with the GI-XRD results. The lamella was further analyzed with TEM-EDS, **Figure 9**, where it was confirmed that metallic Ni was present in the top part of the deposited layer.

The presence of metallic Ni on top of the deposit indicates that Ni had diffused through the entire layer.

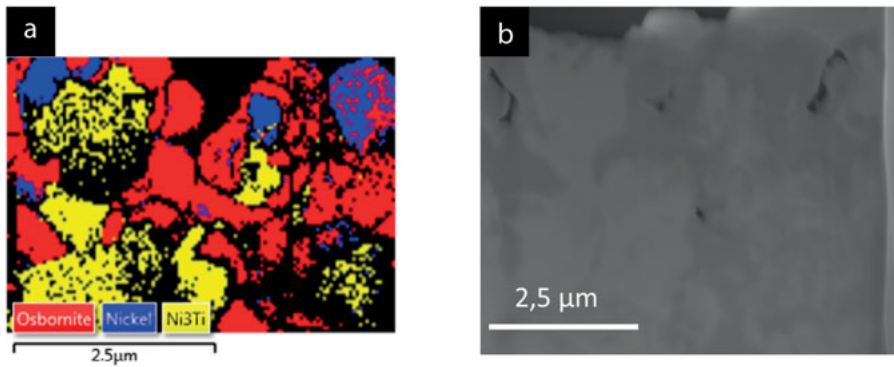


Figure 8. a) TKD map of the top part of the TiN coating on Ni. The red color corresponds to Osbornite (TiN), blue corresponds to metallic Ni, and yellow corresponds to Ni₃Ti. Black areas denote areas with zero solutions. b) SEM cross-section micrograph of the area analyzed using TKD.

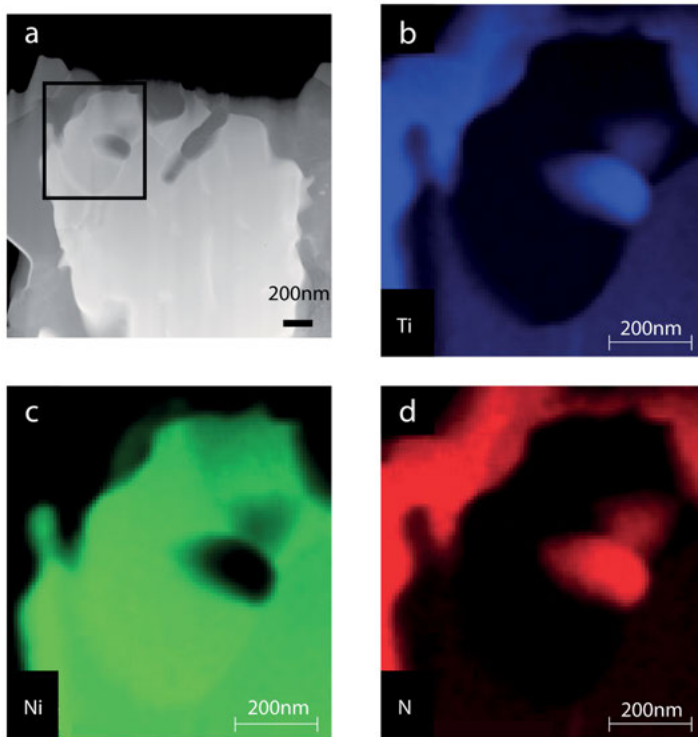


Figure 9. a) STEM-HAADF micrograph of the lamella, depicting the top of the deposited layer. The EDS analysis area is marked with the black rectangle. b-d) EDS maps of Ni, Ti and N respectively.

The apparent activation energies for the depositions on Co and Ni substrates were obtained by making Arrhenius plots of the growth rate as a function of temperatures, see **Figure 10a** and **b** respectively. **Figure 10b** shows that the apparent activation energy for TiN deposition on Co substrates was 90 kJ/mol. This activation energy is in the range that can be expected for a process under surface kinetic reaction control [26].

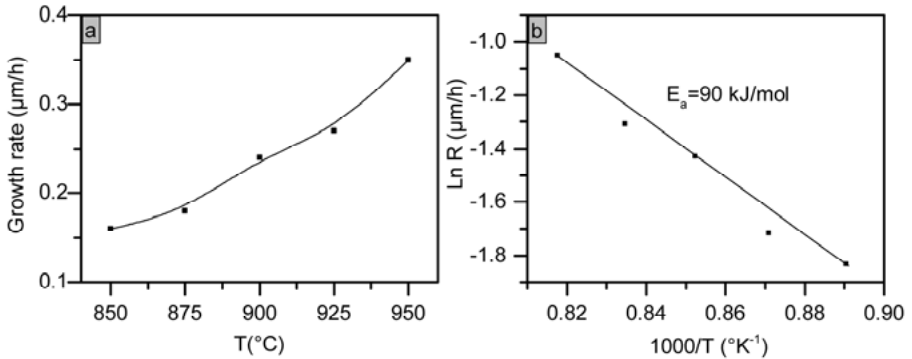


Figure 10. a) Growth rate of TiN deposited on Co as function of temperature. b) Arrhenius plot for TiN deposited on Co. The lines are merely guides for the eye.

The growth rate as a function of the temperature and an Arrhenius plot for TiN deposited on Ni, including a large fraction of Ni_3Ti and small amounts of Ni, are presented in **Figure 11**. In the Arrhenius plot, **Figure 11b**, two linear regions with different slopes can be observed. This indicates a change of the rate-limiting mechanism. However, the film growth process involves three phases, TiN, Ni and Ni_3Ti . The presence of Ni_3Ti and Ni implies diffusion of Ni from the substrate. This means that the film growth depends on two competing processes, diffusion in the solid state and deposition from the gas phase. Both processes have an exponential dependence on the temperature if kinetically controlled. However, the picture is further complicated since the CVD reaction may become mass transport-limited at high temperatures. The change of the apparent activation energy from 40 kJ/mol to 165 kJ/mol above 900 $^{\circ}\text{C}$ thus indicates a change from a mass transport limited reaction to a different type of control.

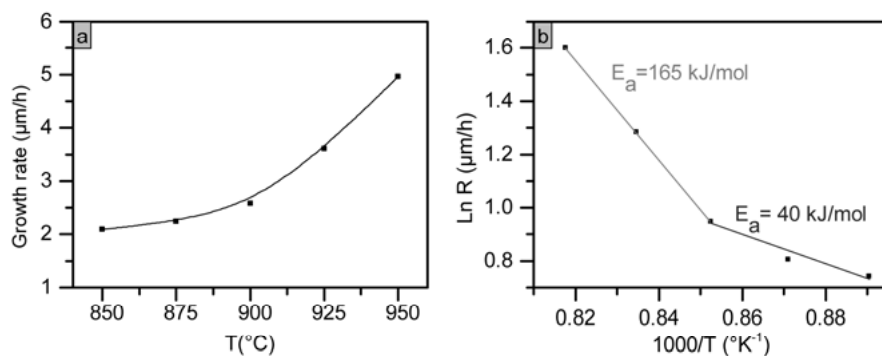


Figure 11. a) The growth rate of Ni_3Ti and TiN deposited on Ni as function of the temperature, b) Arrhenius plot for the deposition of Ni_3Ti and TiN . The lines are merely guides for the eye.

The formation of Ni_3Ti was not predicted by the thermodynamic calculations, leading to the conclusion that the difference between the experimental results and the calculations is caused by kinetic factors. A theoretical study regarding N_2 on different metallic surfaces suggested that the recombination rate of nitrogen yielding N_2 on a Ni surface is higher than the dissociation rate [69]. This implies that there will be a lower surface concentration of atomic N on the Ni surface compared to on Fe and Co . This in turn would lead to a reduction of the TiN formation since the concentration of the rate limiting reactant (N) is low. This could explain why no TiN could be found directly on metallic Ni but on the Ni_3Ti phase, see **Figure 7f** and **Figure 8a**.

When TiN was deposited on Ni substrates at a reduced H_2 partial pressure (and increased N_2 partial pressure) the formation rate of Ni_3Ti was decreased, as shown in paper I. The resulting coating from this deposition was more like those deposited on Co substrates with a similar grain morphology and a dense columnar microstructure, see **Figure 12 a** and **c**. It is shown in **Figure 12 b** and **c** that the growth of intermetallic phases still took place. The protrusions were analyzed by EDS, by which it was found that they consisted mostly of Ni , and possibly also Ti , see **Figure 12d**.

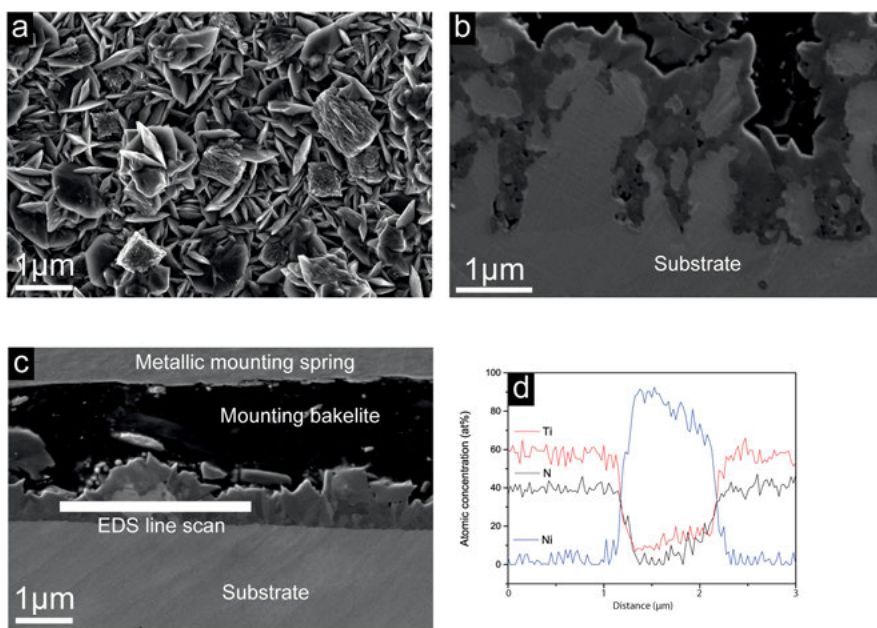


Figure 12. a) Top view micrograph of the coating deposited on Ni using a reduced H_2 partial pressure. b) cross section of the multi-phase area, and c) cross section with the EDS line scan indicated. d) EDS line scans.

Two mechanisms were considered responsible for the decreased Ni_3Ti growth rate. The first assumes that the reduction rate of $TiCl_4$ will drop in the absence of an excess of H_2 as the required energy for Cl removal without H_2 is substantially higher [70,71]. This would cause $TiCl_4$ to be reduced on the surface which would yield more surface reaction steps, which would increase the residence time on the surface of Ni. This in turn may increase the probability for interactions with N on the surface. The second proposed mechanism simply involves the fact that an increased N_2 partial pressure will increase the surface fraction of N. This will increase the probability of surface reactions between Ti and N. Both suggested mechanisms would explain the increase in the growth rate seen for TiN on a Ni surface.

4.2. Kinetics and growth of Ti(C,N)

Ti(C,N) is normally the layer covering TiN on coated WC-Co tools. The role of Ti(C,N) is to provide hardness and also resistance to abrasive wear to the material. Although used for a long time the $TiCl_4 + CH_3CN$ deposition process for Ti(C,N) is not particularly well studied. In papers II and III, kinetics and gas phase modifications of the process were studied.

To study the effects of process modifications and at the same time reduce the probability of chemical interactions with the substrate, an inert substrate was used - single crystal α -Al₂O₃ (001) substrates. Furthermore, to enable measurements of the growth rate profile in the CVD reactor, polished WC-Co substrates were also placed at the center, half radius and the periphery in the bottom, middle and top of the reactor as described in **Figure 1**.

4.2.1. TiCl₄ and CH₃CN series

The growth kinetics of Ti(C,N) was studied in a series involving six experiments at 860 °C and 8 kPa total pressure. The partial pressures of TiCl₄ and CH₃CN were varied, see **Table 1**.

Table 1. Deposition parameters used for kinetic studies of the Ti(C,N) deposition
Gas partial pressures in kPa, total flow rate in l/min.

Sample	H ₂ (kPa)	N ₂ (kPa)	TiCl ₄ (kPa)	CH ₃ CN (kPa)	Total flow rate (l/min)	Deposition time (h)
T1	Balance	0.98	0.11	0.05	82	5
T2/A1	Balance	0.98	0.15	0.05	82	5
T3	Balance	0.98	0.19	0.05	82	5
A1/T2	Balance	0.98	0.15	0.05	82	5
A2	Balance	0.98	0.15	0.06	82	5
A3	Balance	0.98	0.15	0.07	82	5
A4	Balance	0.98	0.15	0.09	82	5

The elemental compositions of the coatings (T1-T3 and A1-A4) were measured by XPS depth profiling, see **Figure 13**. They were close to Ti(C_{0.6}N_{0.4})_{0.8} for all depositions, suggesting that the composition was unaffected by the precursor partial pressures.

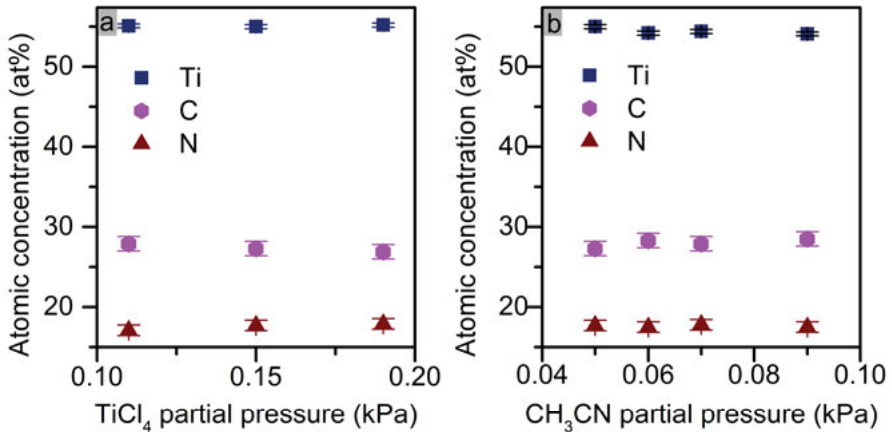


Figure 13. XPS-depth profiling composition of Ti(C,N) as a function of a) The TiCl_4 partial pressure, and b) The CH_3CN partial pressure.

The growth rate of Ti(C,N) as a function of the TiCl_4 partial pressure is shown in **Figure 14a**. It can be seen that the growth rate decreased slightly when the TiCl_4 partial pressure was increased.

The reaction order of TiCl_4 was determined by plotting the logarithm of the growth rate versus the logarithm of the TiCl_4 partial pressure. The resulting log-log diagram is shown in **Figure 14b**. The slope of the line is close to zero, indicating that the reaction order was zero. This is in agreement with previous studies of the reaction kinetics for TiC and TiN depositions [72–74].

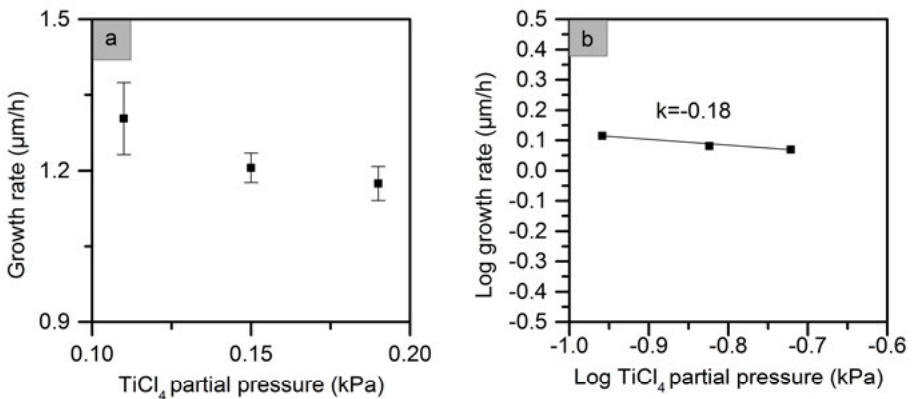


Figure 14. a) Growth rate of Ti(C,N) as a function of the TiCl_4 partial pressure for depositions T1-T3. b) Log-log diagram of the Ti(C,N) growth rate versus the TiCl_4 partial pressure, where the reaction order is indicated by the slope of the line shown in the figure.

The experiments in which the CH_3CN partial pressure was varied, A1-A4, showed a steady increase in the growth rate with increased CH_3CN partial

pressure, see **Figure 15a**. The log-log diagram for the CH₃CN series, see **Figure 15** showed a reaction order close to unity.

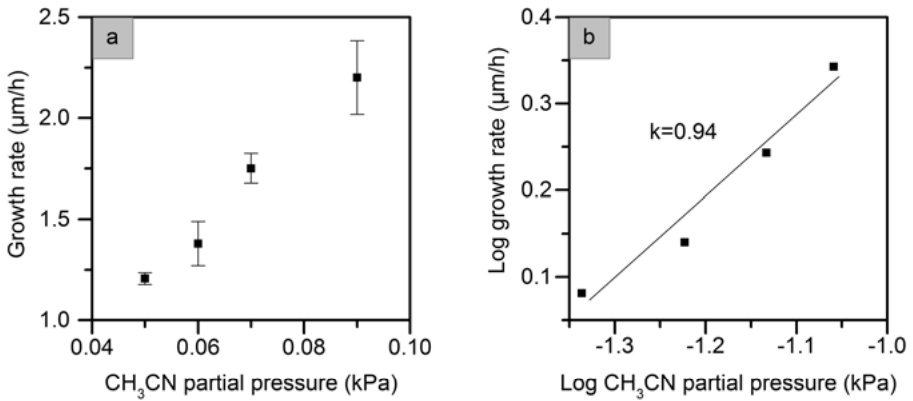


Figure 15. Growth rate of Ti(C,N) as a function of the CH₃CN partial pressure (A1-A4). b) log-log diagram of the Ti(C,N) growth rate versus the CH₃CN partial pressure, the reaction order indicated by the slope of the line shown in the figure.

In summary, the rate determining reactant in CVD of Ti(C,N) from CH₃CN and TiCl₄ was determined to be CH₃CN with a reaction order close to unity. Furthermore, the composition of the coatings was unaffected by the precursor partial pressure.

4.2.2. Nitrogen modified Ti(C,N) deposition

In addition to the kinetic investigations of the Ti(C,N) deposition process, experiments in which the gas phase was modified were also performed. It has been suggested that N₂ additions could increase the growth rate, but no explanation to why this could be the case was offered [75].

Therefore, a series of depositions were made where the N₂ partial pressure was varied. To keep the total gas flow rate constant the same amount of H₂ was removed as the amount of N₂ added. The deposition parameters in the experiments are shown in **Table 2**.

Table 2. Experimental parameters for depositions with varied N_2 partial pressure, $T=830\text{ }^\circ\text{C}$, $P_{\text{tot}}=8\text{ kPa}$, $TiCl_4=0.26\text{ kPa}$, $CH_3CN=0.04\text{ kPa}$, total flow rate= 40 l/min.

Sample	H_2 (kPa)	N_2 (kPa)	Ar(kPa)	Growth rate ($\mu\text{m/h}$)
0	7.7	0	0	1.24
1	6.5	1.2	0	1.52
1A	6.5	0	1.2	1.01
2	4.9	2.8	0	1.43
3	2.8	4.9	0	1.16
4	0.7	7.0	0	0.67
5	0.4	7.3	0	0.24

The growth rate of $Ti(C,N)$ increased as the partial pressure of N_2 was increased up to 2.8 kPa, see **Figure 16**. At higher partial pressures the growth rate decreased. The initially increased growth rate is not straightforward to explain. However, in order to determine if N_2 in some way is active in the reaction, one deposition experiment was made with Ar rather than N_2 , see sample 1A **Table 2**. The growth rate was not increased when using Ar instead of N_2 . This suggests that N_2 participates in the reaction despite the fact that N_2 is considered relatively inert at the temperature used in these depositions ($830\text{ }^\circ\text{C}$) [7,24].

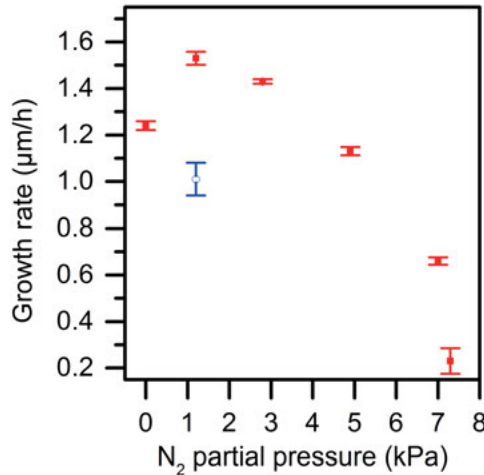


Figure 16. Growth rate of $Ti(C,N)$ on $(001)\alpha\text{-Al}_2\text{O}_3$ as a function of the N_2 partial pressure. The hollow blue circle marks where the experiment in which Ar was used rather than N_2 .

The compositions of the coatings were determined by XPS depth profiling. It is shown in **Figure 17** that the coatings were on the carbon-rich side, corresponding to a composition of $Ti(C_{0.6},N_{0.4})_{0.8}$.

The deposited coatings showed no significantly increased N content (**Figure 17**), except for the coating deposited at the highest N_2 partial pres-

sure. This leads to the conclusion that N_2 affects the growth in some other way than via incorporation in the growing coating.

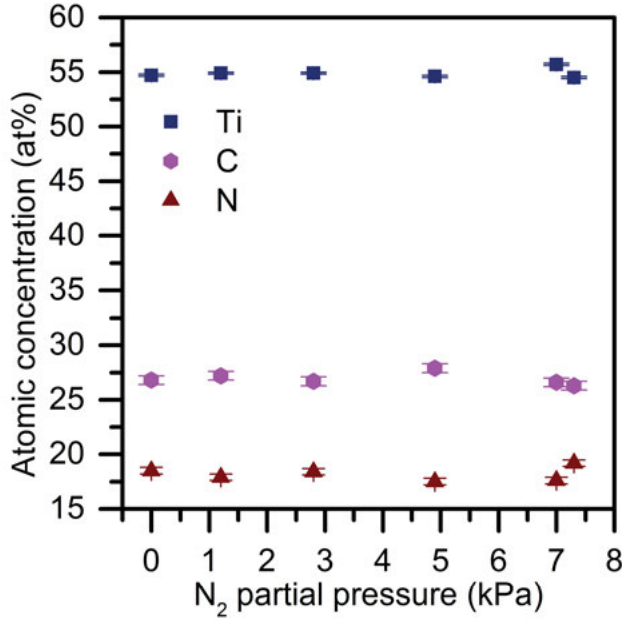


Figure 17. Compositions of all deposited Ti(C,N) layers as a function of the N_2 partial pressure. Ti, C and N are marked in black, red and blue respectively. The error bars represent one standard deviation.

Thermodynamic calculations were used to simulate the gas phase composition as a function of the concentration of added N_2 . These calculations were performed without letting any condensed phases form, thus only simulating the equilibrium in the gas phase. The calculations were done using the same parameters as used in the depositions, see **Table 2**. The results of the thermodynamic calculations, shown in **Figure 18**, suggest that the main species in the gas phase that contribute to the growth of Ti(C,N) are $TiCl_3$, $TiCl_4$, and HCN (CH_4 could be considered quite inert at 830 °C). HCN and NH_3 are the only species significantly affected by the addition of N_2 , which leads to the conclusion that they are probably crucial for the growth of Ti(C,N). Furthermore, the partial pressure of both HCN and NH_3 dropped an order of magnitude when replacing N_2 with Ar, which agrees well with the observed growth rate decrease seen when Ar was used instead of N_2 . Those calculations are marked with stars in **Figure 18**.

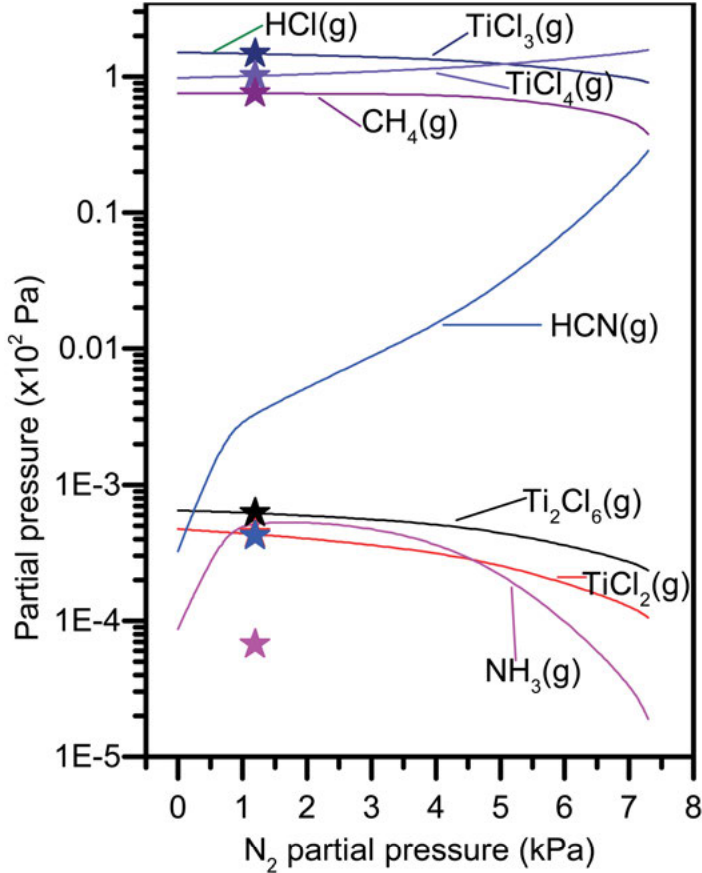


Figure 18. Gas-phase composition as a function of the N_2 partial pressure. Stars of respective color represent calculations in which Ar was added instead of N_2 .

However, it is not believed that NH_3 is a major contributor to $Ti(C,N)$. Should NH_3 take part in the reaction, the resulting coating would most likely be enriched in N as NH_3 would be highly reactive at 830 °C. As none of the deposited coatings had an increased N content, except for the one deposited at the highest N_2 pressure, see **Figure 17**, it is not probable that NH_3 took part in these reactions. Therefore, there is a discrepancy between the experimental results and the thermodynamic calculations. This leads to the conclusion that the formation of NH_3 most likely is kinetically limited. A reasonable explanation is that it is thermodynamically favorable to form NH_3 from N_2 and H_2 and thereby the calculated NH_3 partial pressure will increase when N_2 is added. However, there is a large kinetic barrier not accounted for in the thermodynamic calculations. As NH_3 synthesis from N_2 and H_2 normally

needs high pressures ($101 \cdot 10^2$ kPa) and a catalyst, it is not likely that NH_3 would be produced under the present conditions [76].

The growth rate decrease observed at N_2 partial pressures above 2.8 kPa, see **Figure 16**, was most likely caused by a decreased partial pressure of TiCl_3 caused by the lower H_2 partial pressure at increased N_2 partial pressures. Reduction of TiCl_4 in the presence of H_2 requires significantly less energy than dissociation of TiCl_4 via formation of Cl_2 , which can take place in absence of H_2 [71,77]. This can explain why a low H_2 partial pressure will reduce the growth rate.

In summary, N_2 additions can increase the growth rate of $\text{Ti}(\text{C},\text{N})$ without altering the composition, as long as H_2 is kept in a large enough surplus. An increase of the HCN partial pressure is suggested to be the main mechanism behind the increased growth rate.

4.3. Orientation, microstructure and morphology of $\text{Ti}(\text{C},\text{N})$ and its implications on the mechanical properties.

The orientation, microstructure and morphology of the coatings deposited in the N_2 series, depositions T1-T3 and A1-A4 described in the previous sections were investigated.

4.3.1. Morphology and microstructure of $\text{Ti}(\text{C},\text{N})$

The morphology of the deposited layers was affected by the N_2 additions, as the grain size increased as the N_2 partial pressure was increased, see **Figure 19a-e**. As can be seen, the coatings deposited between 0 and 2.8 kPa N_2 had a majority of ridge-like grains and a fibrous microstructure. The coating deposited at a partial pressure of 4.9 kPa N_2 had a mixture of ridge-like grains and large flat grains and showed a microstructure with significantly larger grains than those of the layers deposited at lower N_2 partial pressures. At even higher N_2 partial pressures, 7 and 7.3 kPa, the layers contained large flat grains, see **Figure 19e** and **f**. These layers showed a similar microstructure to that of sample 3, with large grains. The changed morphology and microstructure indicates a change in preferred orientation of the layers grown at high N_2 partial pressures.

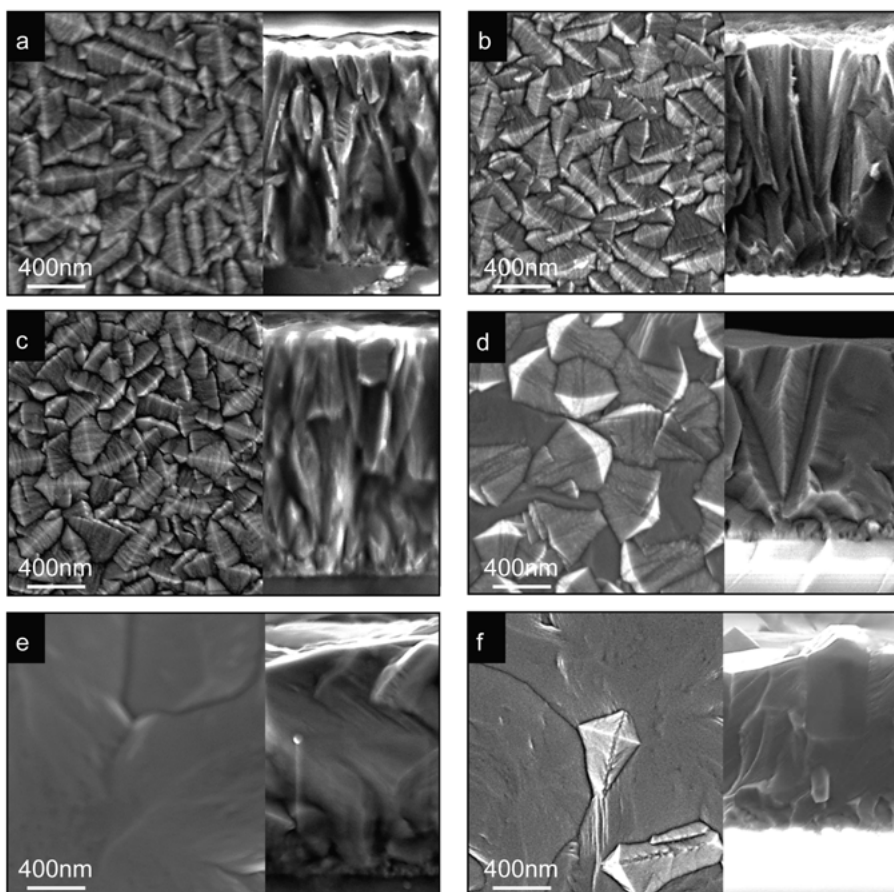


Figure 19. SEM top view and cross section micrographs of the coatings from the N_2 series, sample 0-5 (0-7.3 kPa N_2) in a-f respectively.

For the $TiCl_4/CH_3CN$ series it was found that the microstructure could be altered by changing the $TiCl_4/CH_3CN$ ratio. A $TiCl_4/CH_3CN$ ratio above 2.5 led to a fine-grained fibrous microstructure similar to that of samples 0-2 from the N_2 deposition series (**Figure 19 a-c**).

A $TiCl_4/CH_3CN$ ratio between 1.7 and 2.5 led to a coarse-grained microstructure, similar to that of samples 4 and 5 from the N_2 deposition series (**Figure 19e and f**), as was shown in paper II.

This shows that replacing H_2 with N_2 yields similar effects as adjusting the $TiCl_4/CH_3CN$ ratio. The coarse microstructure was only observed for N_2 partial pressures of 4.9 kPa or above. At these N_2 partial pressures the ratio $TiCl_3/HCN$ is decreasing rapidly, indicating that this is determining the microstructure in both studies, see **Figure 18**.

4.3.2. Orientation

The orientation of the layers was affected by the N_2 partial pressure in a similar way as the morphology and microstructure. The layers grown at lower partial pressures of N_2 (0-4.9 kPa) featured a mixture of orientations, i.e. $\langle 111 \rangle$, $\langle 211 \rangle$, and $\langle 311 \rangle$, see **Figure 20**. The layers grown at N_2 partial pressures of 7 and 7.3 kPa exhibited a single $\langle 111 \rangle$ orientation. Furthermore, for the deposition at the highest N_2 partial pressure, a TiN phase was co-deposited, see **Figure 20**. The co-deposition of TiN is in accordance with the increased N content observed in this layer, see **Figure 17**. Due to an absolute overlap between the (333) and (511) reflections, a $\langle 511 \rangle$ orientation cannot be excluded. The presence of the $\langle 511 \rangle$ orientation can be investigated using pole figure measurements as there is no overlap in those measurements.

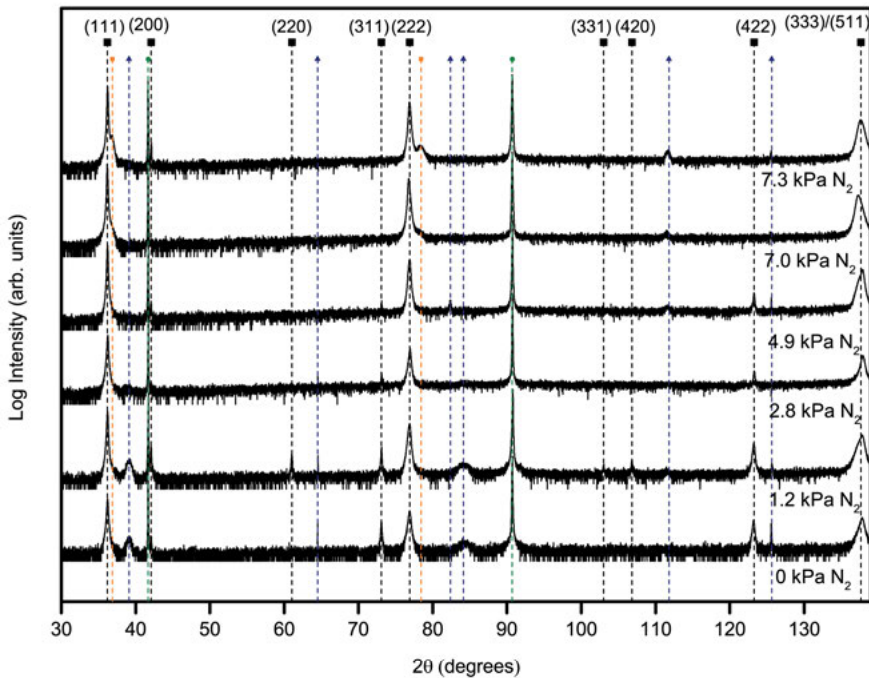


Figure 20. θ - 2θ diffractograms of samples deposited with 0-7.3 kPa N_2 partial pressures. Ti(C,N) peaks are marked with (hkl), TiN peaks indicated by orange squares, instrument artifacts (Al from the sample holder) indicated by blue triangles, while sapphire (006) and (0012) peaks are indicated by green circles.

The orientation of layers deposited in the $TiCl_4/CH_3CN$ series followed the same trends as the layers from the N_2 series. The layers with fine grains and fibrous microstructures exhibited a mixture of orientations whereas the layers with large grains featured a $\langle 111 \rangle$ orientation. The degree of orientation in the layers grown in the $TiCl_4/CH_3CN$ series was investigated by rocking

curve measurements. It was found that the layers grown at $\text{TiCl}_4/\text{CH}_3\text{CN}$ ratios between 1.7 and 2.5 showed the highest degree of $\langle 111 \rangle$ orientation, with a ω -peak FWHM of $0.3\text{-}0.5^\circ$. The layers grown with a mixture of orientations had a lower degree of orientation for both the $\langle 111 \rangle$ orientation and $\langle 211 \rangle/\langle 311 \rangle$ orientations, with ω -peak FWHM of 1.7° for the $\langle 111 \rangle$ orientation, $2.5\text{-}4.7^\circ$ for the $\langle 211 \rangle$ orientation and $5.6\text{-}5.9^\circ$ for the $\langle 311 \rangle$ orientation. This shows that the precursor ratio strongly affects both the microstructure and the preferred orientation.

In order to determine the in-plane orientation relationship between the substrate and the deposited layers in the N_2 series, pole figure measurements were used. All the deposited layers showed in-plane ordering (epitaxy), see **Figure 21**. Furthermore, it can be seen that the investigated layers had crystal twinning, hence the presence of twice the amount of reflections for each orientation compared to what can be expected for a cubic material. Crystal twinning is common in these systems and is more or less always present [46,78]. The layers deposited below 7 kPa N_2 show pole figures with three sets of reflections corresponding to three orientations, also visible in the θ - 2θ measurements, **Figure 21a-d**. The reflections are marked d1, d2, and d3 for $\langle 511 \rangle$, $\langle 111 \rangle$, and $\langle 211 \rangle$ respectively. The twins are marked with td1, td2 and td3 for the respective orientations. The layers deposited at higher N_2 partial pressures showed pole figures with one (7 kPa N_2) and two (7.3 kPa) sets of reflections, respectively, corresponding to $\langle 111 \rangle$ and $\langle 511 \rangle$, see **Figure 21e and f**.

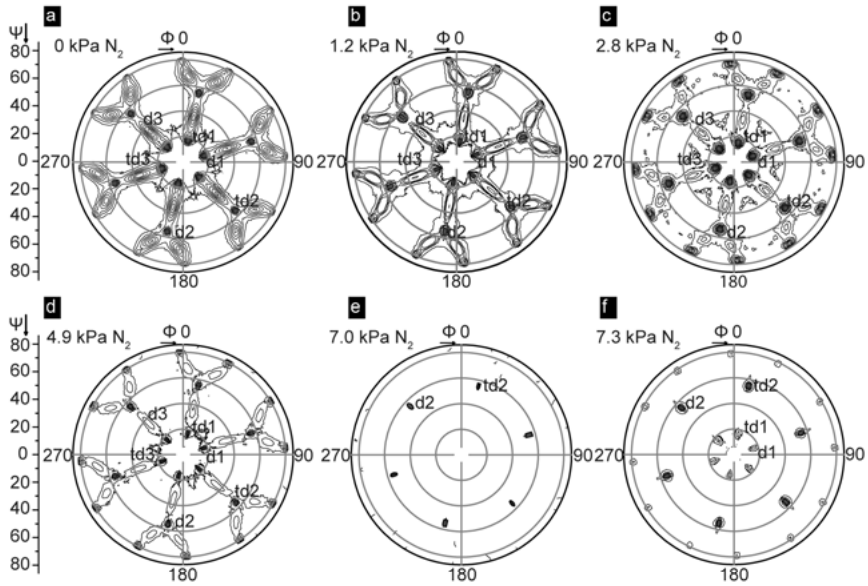


Figure 21. *Ti(C,N)(200)* pole figures for samples deposited at p_{N_2} partial pressures between 0 and 7.3 kPa (samples 0-5) presented in a-f, respectively. All samples show evidence of crystal twinning, hence the six-fold symmetry.

To determine the epitaxial relation to the substrate, reference pole figures were measured on the (104) plane in the α - Al_2O_3 . From the obtained pole figures the orientation (epitaxial) relationships between the layer and substrate could be determined as well as the lattice mismatch. The relation between the dominant $\langle 111 \rangle$ orientation and the substrate was determined to $Al_2O_3(001)[110]/Ti(C,N)(111)[1-21]$ for the reflection d2 and $Al_2O_3(001)[-1-10]/Ti(C,N)(111)[-12-1]$ for the reflection td2. This is in agreement with previous experiments involving CCP crystals on α - Al_2O_3 [79]. The degree of mismatch was calculated to be 10.3 % for the experimentally determined epitaxial relation along the $Al_2O_3[110]$ direction and 10.4 % along the $Al_2O_3[-110]$ direction.

4.3.3. Texture forming mechanism in Ti(C,N) deposition

From the Ti(C,N) growth investigations it was found that a dominant $\langle 211 \rangle / \langle 311 \rangle$ orientation develops when the $TiCl_4/CH_3CN$ ratio and the surplus of H_2 are large.

The nucleation and growth of a specific preferred orientation is most often hard to explain without insight into the microstructure as well as the surface chemistry of the precursor species. Growth of a coating with NaCl/CCP-type structure on a sapphire (001) surface has been shown to give $\langle 111 \rangle$ preferred orientation in several investigations [79–81]. This has been shown to be the

result of the close-packed surface on the sapphire (001) matching the close-packed {111} surfaces in the cubic coating. In Ti(C,N) the {111} surfaces are close packings of either Ti or C/N, shown in **Figure 22a**. However, the $\langle 211 \rangle$ and $\langle 311 \rangle$ orientations deposited at high TiCl_4 partial pressures are not as straightforward to explain. The fact that the preferred orientation changes with the $\text{TiCl}_4/\text{CH}_3\text{CN}$ molar ratio or upon reduced H_2 partial pressure suggests that a specific growth or adsorption mechanism becomes dominant, thus generating the preferred orientation.

For a $\langle 211 \rangle$ oriented Ti(C,N) coating deposited from TiCl_4 and CH_3CN on WC/Co substrates, the microstructure has been investigated by TEM [46]. The microstructure agrees well with that of the $\langle 211 \rangle/\langle 311 \rangle$ oriented coatings grown in both the $\text{TiCl}_4/\text{CH}_3\text{CN}$ series and the N_2 series on sapphire (001) substrates. The morphology of the $\langle 211 \rangle$ oriented grains obtained in this thesis, see **Figure 22c**, is in agreement with the previously shown morphology [46].

The grains in the $\langle 211 \rangle$ oriented coatings shared a {111} twin plane, see **Figure 22b**. The twin plane was a Ti plane [46]. Every second plane directed in parallel with the surface normal in the crystal was a Ti {111} plane. These Ti planes were separated by C/N planes also in parallel with the surface normal. To grow this microstructure the growth rate of the twin plane and the Ti planes must be higher compared to the growth rates in other directions.

As the reaction order of CH_3CN was determined to be unity, CH_3CN is assumed to be the rate determining reactant. As such, surfaces with sites that can provide rapid dissociation of the C-N triple bond will be favored during growth, leading to growth in that preferred orientation. The sites between the adsorbed TiCl_x , described in **Figure 22b**, provides possibilities of interaction between HCN (assumed to be formed by homogeneous reactions from CH_3CN) and four Ti atoms simultaneously. It has previously been shown that dissociation of HCN is strongly favored on surfaces that provide more than one bond-forming possibilities [82], thereby strengthening the suggested texture forming mechanism when CH_3CN is used as the C and N precursor for Ti(C,N). The growth texture will then be characterized as a $\langle 211 \rangle$ fiber texture.

The angle between the $\langle 311 \rangle$ and $\langle 211 \rangle$ orientations was about 10° and it has previously been shown that the two orientations are co-existing, in the respect that they both appear when the $\text{TiCl}_4/\text{CH}_3\text{CN}$ molar ratio is high (two or higher) [17,46]. Both directions also lies in the {111} planes. As such it is likely that they are driven by the same mechanism, i.e. the high TiCl_4 partial pressure drives the formation of {111} twinning planes 90° with respect to the surface (tilted 10° in the $\langle 311 \rangle$ case). The $\langle 311 \rangle$ orientation could possibly be the result of a stacking fault during the nucleation of the {111} Ti twinning planes and thus the 10° tilt from the $\langle 211 \rangle$ orientation.

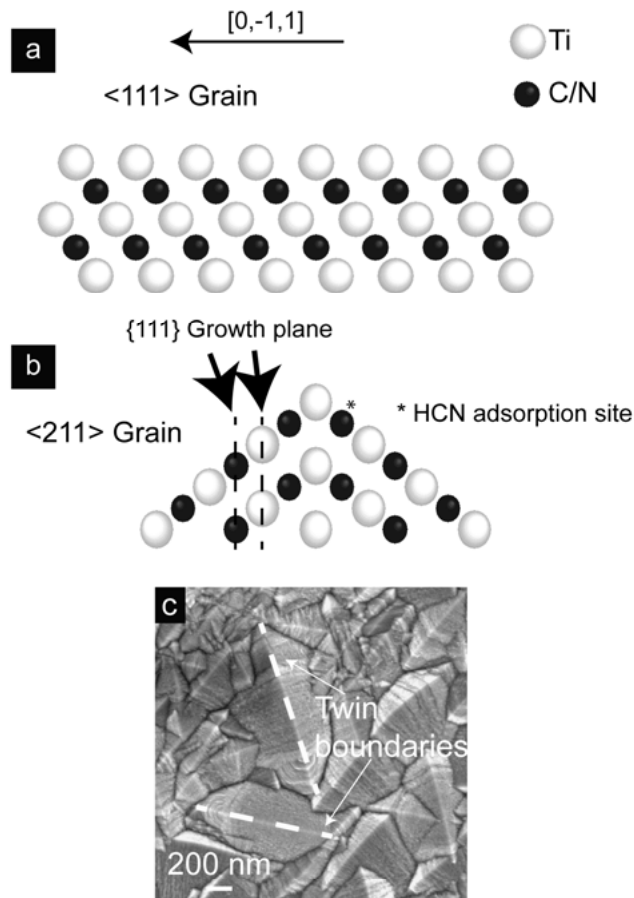


Figure 22. a) Schematic cross section of a $\langle 111 \rangle$ grain, and b) schematic cross section of a $\langle 211 \rangle$ grain. Both a and b viewed along the $[0-11]$ direction. c) example of top view of $\langle 211 \rangle$ oriented grains and twinning planes indicated by dashed red lines.

4.3.4. Implications of the orientation and microstructure on the Ti(C,N) hardness

The hardness of the coatings deposited with added N_2 was determined through nanoindentation as described in paper III. The hardnesses of all the deposited coatings are shown in **Figure 23**. The coatings deposited with N_2 partial pressures below 7 kPa had hardness values in the range of 19-24 GPa, which is in accordance with previous studies on CVD deposited Ti(C,N) [15,16,83–85]. The coatings deposited at 7 and 7.3 kPa N_2 partial pressures attained a hardness exceeding the previous reports, i.e. 36-37 GPa.

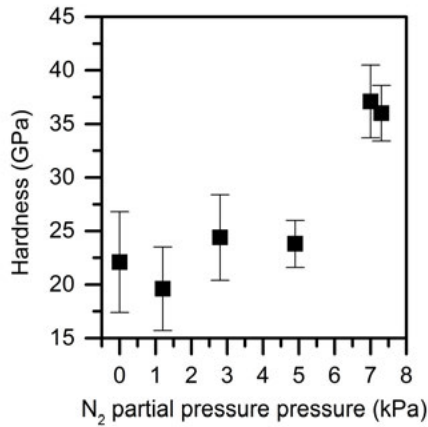


Figure 23. Hardness as a function of the N_2 partial pressure. The error bars represent one standard deviation.

The hardness of the coatings from depositions T1-T3 and A1-A4 were in agreement with those from the N_2 series. The coatings with a mixture of orientations and fine grains (T2/A1 and T3) had a hardness in the range of 23-29 GPa, see **Figure 24a** and **b**, while the coatings with large grains and $\langle 111 \rangle$ orientation were in the range 33-40 GPa. Furthermore, the Young's modulus of these coatings was stable around 600 GPa regardless of the coating hardness.

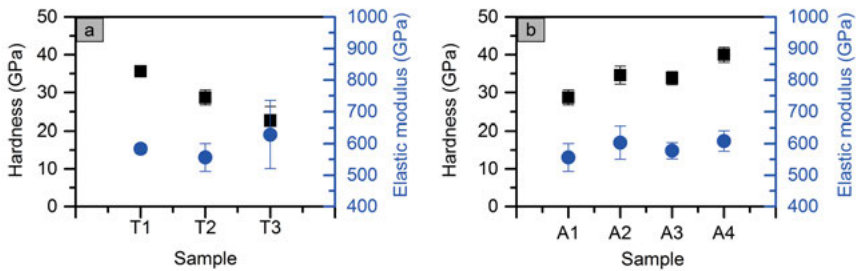


Figure 24. Hardness and Young's modulus measurements via nanoindentation of the coatings with a) varied $TiCl_4$ partial pressure, and b) varied CH_3CN partial pressure.

Previous reports of $Ti(C,N)$ with increased hardness all indicated an increased carbon content, $Ti(C_{0.7},N_{0.3})$, which could explain the increased hardness [85]. As shown earlier in this thesis, the carbon content of the examined coatings was constant with the employed experimental parameters, see **Figure 13** and **Figure 17** respectively. Thus, the increased hardness of the coatings in this thesis cannot be attributed to the presence of a more carbide-rich phase. As mentioned before, the grain size of the coatings with a

high hardness was larger than that of the softer coatings, thus ruling out grain size hardening as well [86].

Compressive residual stress is known to increase the hardness of films deposited by sputtering [41,87]. The state of stress was determined by measurements of the cell parameter of one plane parallel to the surface, (111), and one plane 90 ° with respect to the surface, (422). By using Hooke's law and the elastic modulus determined by nanoindentation (632 GPa and 600 GPa for sample 0 and 4 respectively) the state of residual stress can be determined [49]. The measured unit cell parameters and state of stress are shown in **Table 3**.

Table 3. Cell parameters and state of stress in the examined Ti(C,N) coatings

Sample	N ₂ deposition pressure (kPa)	Cell parameter (111) plane (Å)	Cell parameter (422) plane (tilted 90°)	Residual stress (GPa)
0	0	4.2917	4.2931	0.21
4	7.0	4.2947	4.2834	-1.6

From those measurements it can be seen that the reference layer, deposited with no N₂, showed a virtually stress-free condition with only a slight tensile stress of 0.21 GPa, whereas the coating deposited with a high N₂ partial pressure exhibited compressive stresses of about 1.6 GPa. The state of compressive stress is most likely caused by the large mismatch calculated from the epitaxial relations. This would also explain why the coating deposited without N₂ had no compressive stress. As this coating changes orientation from <111> to <211> the strain induced by the substrate is most likely reduced. Furthermore, it can be seen in the pole figures, **Figure 21**, that the coatings deposited at N₂ partial pressures below 7 kPa exhibit wider peaks. This corresponds to a slightly lower degree of in-plane ordering and thus a lower strain which thereby relieve the stress. Nevertheless, such small compressive stress is most likely not the sole contributor to the increased hardness. Therefore, additional investigations were needed to identify the hardening mechanism.

4.3.5. Hardening mechanism

To further investigate the difference in hardness, two additional depositions were made. One deposition with the same parameters as for sample 0 in **Table 2** (reference) and one deposition with the same parameters as for sample 4 in **Table 2** (<111> oriented). TEM lamellas were made for both coatings, the TEM analysis of the as-deposited reference coating is presented in paper **IV**. In addition to the TEM analyses the degree of orientation for both coatings was investigated by rocking curve measurements. The <111> oriented coating only showed a ω -peak for the (111) plane, with a FWHM of 0.3 °.

The reference coating showed ω -peaks for the (111), (311) and the (422) planes, with FWHM values of 0.9° , 5° and 4.2° respectively. This shows that the $\langle 111 \rangle$ oriented coating had a significantly higher degree of orientation than the reference coating.

A STEM-BF overview micrograph of the as-deposited $\langle 111 \rangle$ oriented coating is shown in **Figure 25a**. It can be seen that the top 20-30 nm of the coating (indicated in **Figure 25a**) had a high density of defects. Further analyses of the defect-dense surface layer of the coating are shown in **Figure 25b** and **c**. The HR micrograph shown in **Figure 25b** shows two distinct zones in the top 100 nm of the coating. The zone on the top shows bent crystal planes, see **Figure 25c** (marked with a dashed line), indicating a compression of the crystal. The Fourier transform (FFT) from this area, see **Figure 25d**, shows that the (1-11) and (002) diffraction spots are slightly elongated, indicating a disturbed lattice. The FFT from the zone beneath the defect enriched zone, see **Figure 25e** shows no signs of a disturbed lattice. The defect rich surface layer can prevent buildup and movement of dislocations and thus increase the hardness and prevent crack propagation.

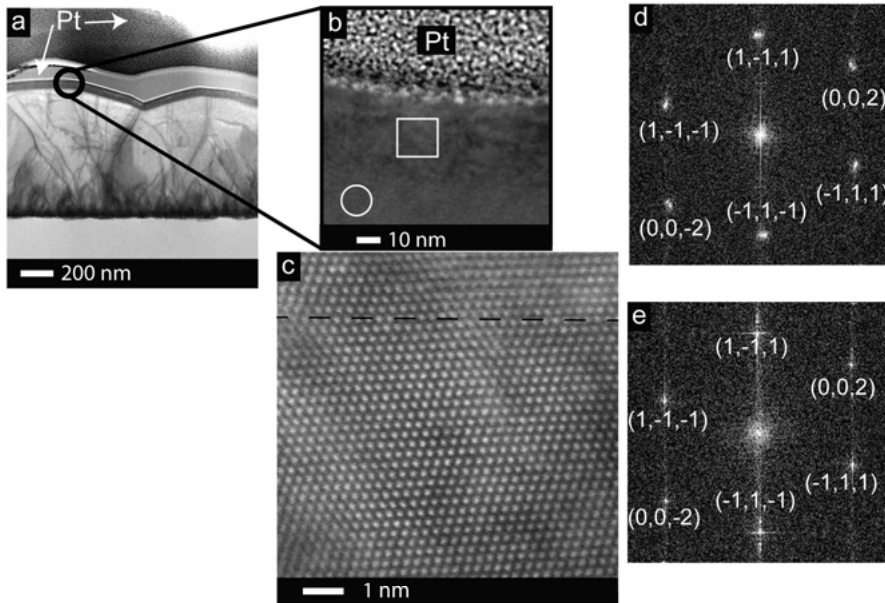


Figure 25. a) STEM-BF overview micrograph of the as-deposited $\langle 111 \rangle$ oriented sample, with the defect rich surface region indicated in figure. b) HR-STEM-HAADF micrograph of the region marked in a, with the area for the FFTs in d and e indicated by a square and a circle respectively. c) HR-STEM-HAADF of the area marked in b. Note the bent crystal plane indicated by the dashed line. d) The FFT of the area marked by a square in c, e) The FFT of the area marked by a circle in c. The zone axis was $[110]$.

To investigate the deformation mechanism for both coatings two samples were subjected to nanoindentation with a large load (68 mN). The large load was chosen to make an indent visual in the FIB to enable a lift-out of TEM lamellas from the indented area. The SEM micrographs of the indents are shown in **Figure 26**, where a clear difference in deformation can be seen. The indent is clearly visible in the reference sample, **Figure 26a**, where entire grains are crushed. Furthermore, cracks can be seen in and around the indent. For the $\langle 111 \rangle$ oriented coating the indent was barely visible, see **Figure 26b**, however, cracks can be seen in connection to the indent.

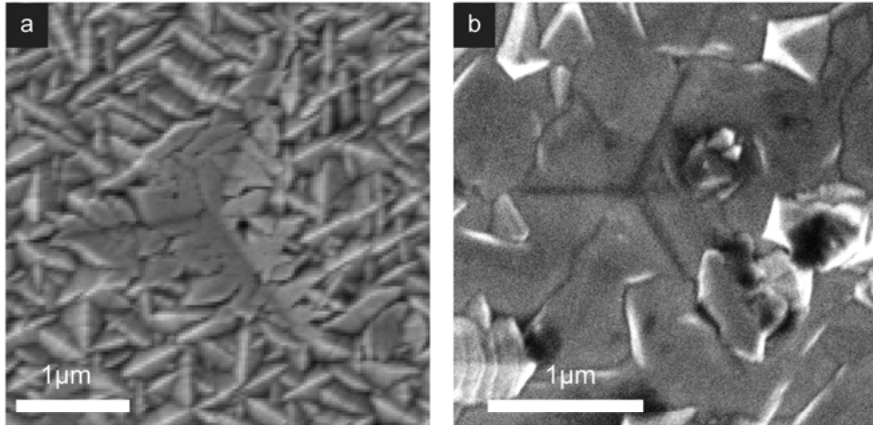


Figure 26. Coating surface after exposure to a large load (≤ 68 mN) for a) a reference coating, and b) a $\langle 111 \rangle$ oriented coating.

The cross-section of the indented area on the reference coating is shown in **Figure 27**. Several cracks, both in the grain boundaries (intergranular) and traversing grains (transgranular) can be seen directly below the indented area. The intergranular cracks cut all the way through the coating down to the substrate. Furthermore, cracks were observed to transverse the columnar grains, splitting the grains in half. These cracks appeared at an approximate angle of 60° with respect to the growth orientation, which could be assumed to be either $\{100\}$ or $\{110\}$ planes, both of which are common cleave planes in a NaCl type structure [86].

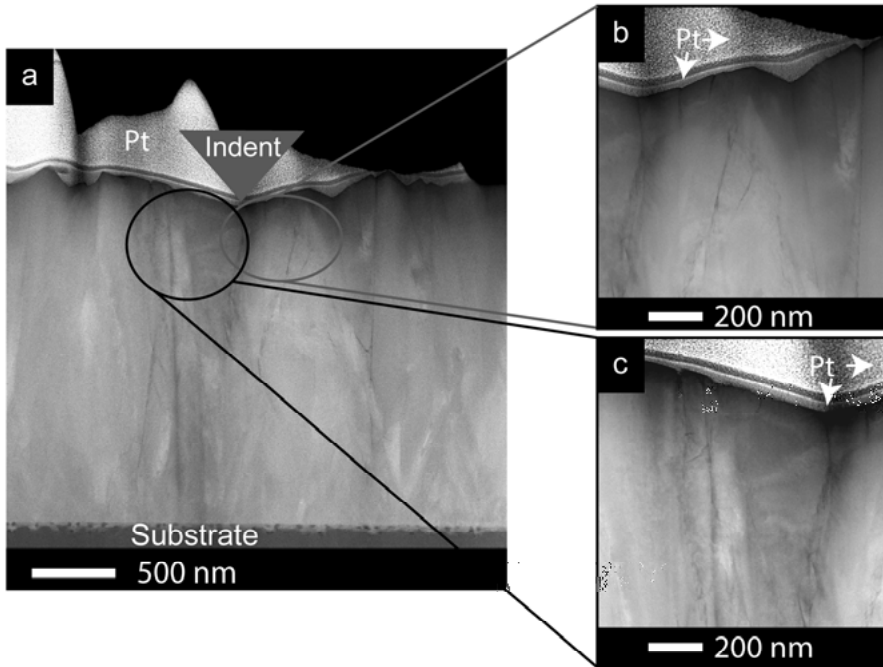


Figure 27. STEM – HAADF micrographs for the indented reference sample: a) overview of the indented area, with the indent indicated in the figure, b) intergranular and transgranular cracks on the right side of the indent, c) intergranular and transgranular cracks of the left side of the indent.

The $\langle 111 \rangle$ oriented coating showed a cross section with fewer cracks compared to the reference coating, see **Figure 28**. Similar to the reference coating, intergranular cracks were found, as indicated in the figure. In contrast to the reference coating, no cracks were found directly beneath the indent. Furthermore, no trans-granular cracks could be observed within the $\langle 111 \rangle$ oriented coating.

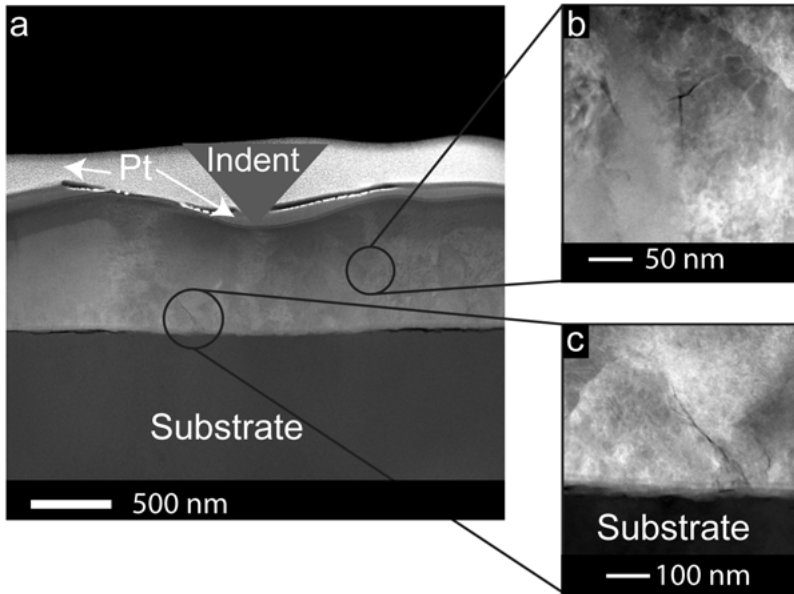


Figure 28. STEM – HAADF micrographs for the indented $\langle 111 \rangle$ oriented sample: a) overview of the indented area, with the indent indicated in the figure, b) grain boundary and t cracks on the right side of the indent, c) grain boundary cracks of the left side of the indent.

A more detailed analysis of the deformation zones of both samples is presented in paper IV. Based on the results from the deformation study and previous studies [88,89], it was found that two different slip systems were activated, the $\{110\}\langle 110 \rangle$ system and the $\{111\}\langle 110 \rangle$ system. However, due to the massive formation of tangles of dislocations it was impossible to determine which of the two systems that was the primary one.

The $\{110\}\langle 110 \rangle$ slip system is 90° with respect to the surface/applied load for the $\langle 111 \rangle$ oriented coating and is therefore not activated. This is not the case for the $\langle 211 \rangle$ oriented coating. Thus only the $\{111\}\langle 110 \rangle$ slip systems will be active for the $\langle 111 \rangle$ oriented coating. Activating dislocations on the $\{111\}\langle 110 \rangle$ slip systems requires a higher critical shear stress compared to activation of the $\{110\}\langle 110 \rangle$ slip system. This leads to an increased hardness for the $\langle 111 \rangle$ oriented coating. In addition, the $\{110\}\langle 110 \rangle$ slip system has only two independent systems, which is not enough to allow for the deformation of a polycrystalline coating, therefore, cracking is more likely [90]. The hardening mechanism and the cracking behavior of the coatings can hence be summarized based on the following points:

- For the $\langle 111 \rangle$ oriented coating, a local surface hardening caused by a buildup of defects was found. The defect buildup in the surface region can serve to prevent crack propagation and increase the coating hardness.
- For the $\langle 211 \rangle$ oriented coating, a majority of the load is applied parallel to a slip plane. As slip planes parallel to the applied load are not activat-

ed, cracking will occur when the applied load exceeds the cohesion strength of the weakest points in the coating. The grain boundaries of the $\langle 211 \rangle$ oriented coating are parallel with the $\{111\}$ planes which makes cracking along such grain boundaries likely. This results in cracks cutting through the entire $\langle 211 \rangle$ oriented coating.

- As a result of the higher degree of orientation, the grain boundaries in the $\langle 111 \rangle$ oriented coating are more coherent than the grain boundaries for the $\langle 211 \rangle$ oriented coating. This could possibly allow for dislocation slip across grain boundaries in the $\langle 111 \rangle$ oriented coating, where this is much less likely in the $\langle 211 \rangle$ oriented coating.
- As an additional result of the misorientation, the applied load will cause both deformation and shear in the columns beneath the indent. This resulted in columns that were split in half in the deformation zone of the $\langle 211 \rangle$ oriented coating, whereas cracks only were observed in the grain boundaries for the $\langle 111 \rangle$ oriented coating.

The combination of these suggested mechanisms can explain the increased hardness of the $\langle 111 \rangle$ oriented coating and also explains why it is less likely to crack than the $\langle 211 \rangle$ oriented coating.

4.4. Tribology of Ti(C,N)

As it was shown that Ti(C,N) coatings with different orientations, $\langle 111 \rangle$ and $\langle 211 \rangle$, had significant differences regarding deformation and crack resistance, there was an interest to also study the tribological properties of such coatings. Two coatings from the depositions in paper II were chosen: depositions T1 and T3. The surface roughness was measured by optical profilometry and determined to be 140 nm and 20 nm for samples T1 and T3 respectively. The grain size of coating T3 was estimated to 100-200 nm and several microns for the coating T1, see **Figure 29**. The hardness of both coatings was measured by nanoindentation, see **Figure 24**, to be 36 and 23 GPa for T1 and T3 respectively.

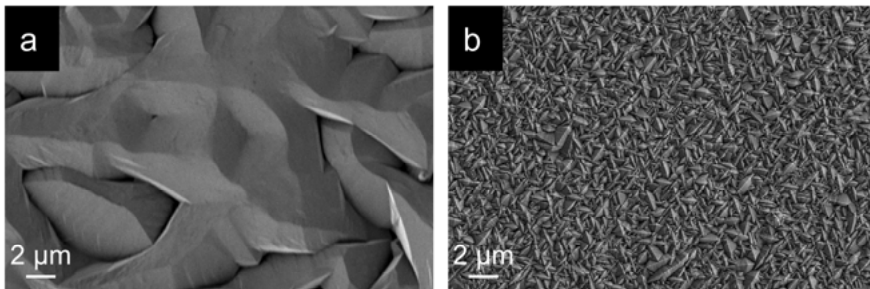


Figure 29. SEM top view micrographs of a) a harder coating (T1), and b) a softer coating (T3).

4.4.1. Microabrasion tests

The abrasion resistance of both coatings was tested with microabrasion. Two different particle sizes were used for the abrasive diamond particles (6 and 1 μm). Abrasion using 6 μm particles showed that the harder coating of sample T1 had a higher wear rate compared to the softer coating of sample T3, **Figure 30**. Micro-chipping was found to be the dominating wear mechanism for the harder coating, **Figure 31a**. The softer coating had a wear mechanism dominated by micro-cutting, **Figure 31b**. Abrasion with 1 μm diamond particles gave the opposite results as the softer coating had a higher wear rate than the harder coating, **Figure 30**. The wear of the harder coating was dominated by micro-chipping, see **Figure 32a**, however less pronounced than for abrasion with 6 μm diamonds. Micro-cutting was found to be the main wear mechanism for the softer coating, see **Figure 32b**.

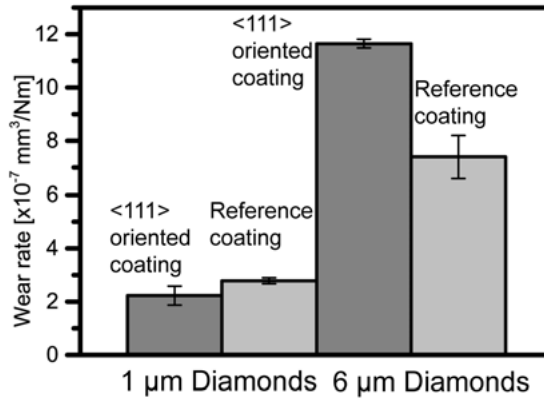


Figure 30. Microabrasion wear rate for both coatings and particle sizes.

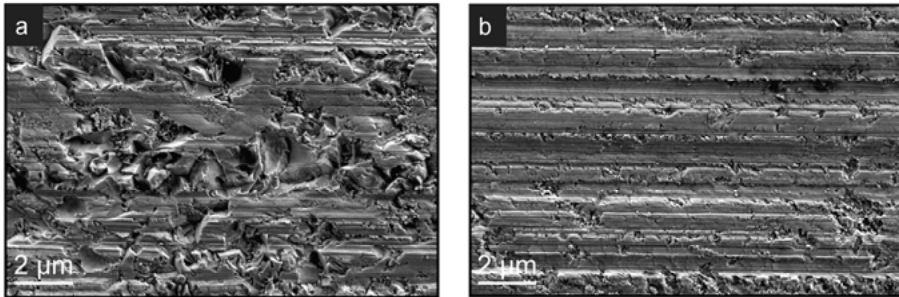


Figure 31. SEM micrographs of the wear scars after initial contact with 6 μm diamonds for a) the harder coating, and b) the softer coating.

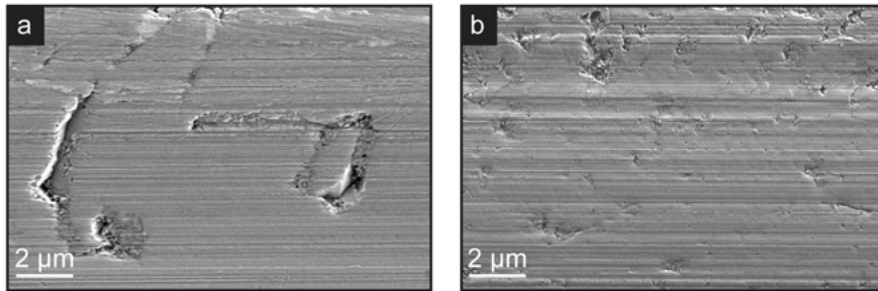


Figure 32. SEM micrographs of the wear scars after initial contact with 1 μm diamonds a) the harder coating, and b) the softer coating.

The fact that the harder coating had a higher wear rate than the softer coating in the abrasion testing using 6 μm particles is somewhat counterintuitive, since harder materials typically exhibit a higher resistance to abrasive wear [91]. The increased wear rate for the harder coating could be explained by considering the relationship between the coating grain size and the size of the abrasive particles.

The grain size in the softer coating was in the range of 100-200 nm. Thus the grain size of the softer coating was significantly smaller than the used abrasive particles, hence the similar wear mechanisms for both 6 and 1 μm diamonds. On the contrary, the harder coating had a grain size of several microns. This means that a change of abrasive particle size changes the relationship between particle size and coating grain size to a large extent. Small abrasive particles cut the surface in a smooth manner, while the larger diamond particles were of about the same size as the coating grains. Thus pronounced micro-chipping occurred where entire grains from the coating were torn out. Furthermore, the increased surface roughness of the harder coating compared to the softer coating, 140 and 20 nm respectively, can further increase the tendency to micro-chipping. Also, the diamond particles are more likely to get lodged between the grains of the harder coating and generate a high local shear stress. As micro-chipping is a more aggressive type of wear than micro-cutting it is reasonable that the coating with large grains had a higher wear rate with 6 μm diamond particles.

4.4.2. Scratch tests

The adhesion and cracking behavior of both the harder and the softer coatings was characterized by scratch testing using a 200 μm Rockwell indenter. The critical loads, L_{c1} and L_{c2} , described in section 3.7.3 were determined by acoustic emission (AE) and SEM respectively.

A representative AE signal and an optical overview image from the scratch testing of the harder coating are shown in **Figure 33a** and **b** respectively. A significant increase of the AE signal occurred after roughly 0.6 mm

of sliding, corresponding to a normal load of about 10 N. The increase in the AE signal corresponded to the onset of cracking of the coating, Lc_1 . A SEM micrograph of the wear at Lc_1 is shown in **Figure 33c**. It is shown that the original grain morphology was preserved, thus no significant deformation occurred. However, cracks were formed as indicated by the AE signal.

It was determined by SEM that Lc_2 was 37 N, which corresponded to a sliding distance of roughly 2.2 mm. The area corresponding to Lc_2 is shown in **Figure 33d**. Severe deformation in the wear track can be observed as well as cracks extending outside the wear track. In addition to the critical loads, the friction between the diamond indenter and the coating was determined in the area where no significant AE occurred (0-0.2 mm). The friction coefficient between the indenter and the coating in the investigated area was 0.11.

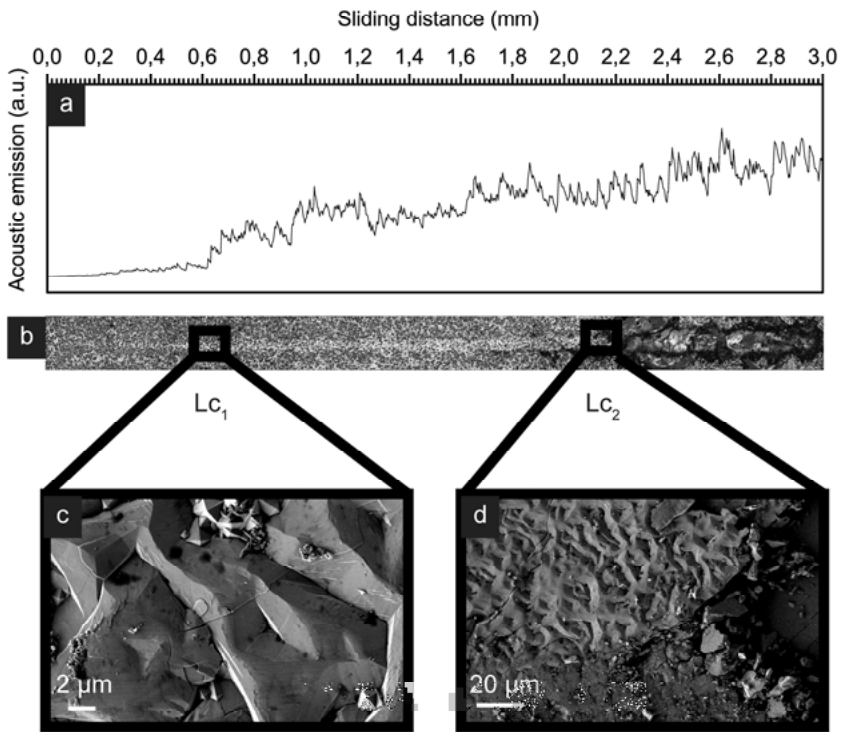


Figure 33. Scratch test of the harder coating: a) representative AE signal, b) optical micrograph overview of the 3 mm wear track, where the positions for Lc_1 and Lc_2 are marked, c) SEM micrograph of the wear at Lc_1 , d) SEM micrograph of the wear at Lc_2 .

The AE signal and optical overview image from the scratch testing of the softer coating are shown in **Figure 34a** and **b** respectively. Lc_1 was determined from the increase in the AE signal after 0.5 mm of sliding. This corresponds to a normal load of 8 N. A SEM micrograph of the wear track at Lc_1 is shown in **Figure 34c**. It can be seen that the coating was plastically de-

formed in the wear track and that cracks were formed both in and outside of the wear track.

Lc_2 was determined to 27.5 N by SEM analysis, corresponding to a sliding distance of 1.6 mm. The wear at Lc_2 is shown in **Figure 34d**. Plastic deformation is shown in the wear track. The friction coefficient between the indenter and the coating between 0 and 0.2 mm was 0.12.

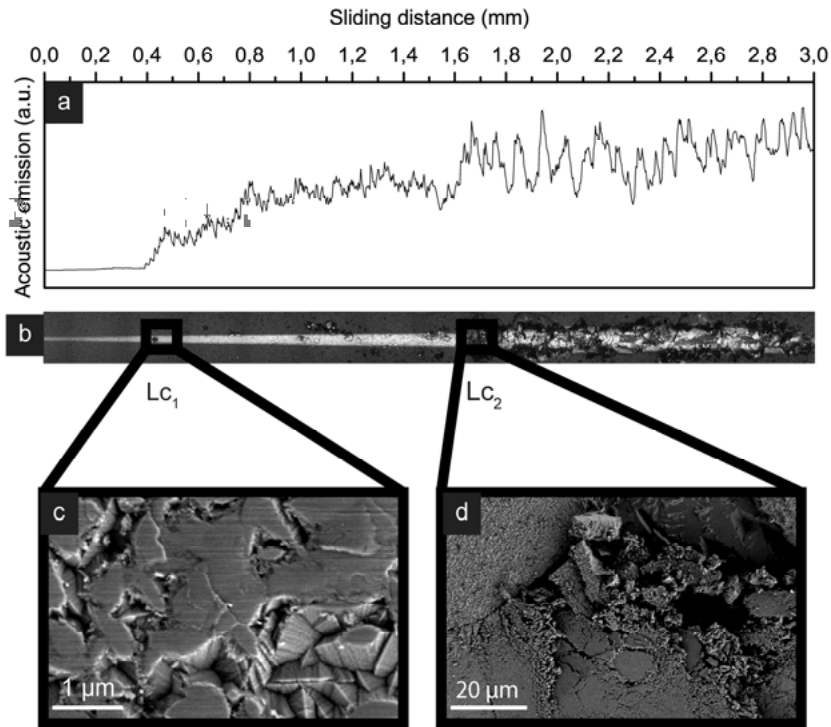


Figure 34. Scratch test of the softer coating: a) representative AE signal, b) optical micrograph overview of the 3 mm wear track, with the positions for Lc_1 and Lc_2 marked in the image, c) SEM micrograph of the wear at Lc_1 , d) SEM micrograph of the wear at Lc_2 .

The scratch test of both coatings clearly showed that the harder coating was superior to the softer coating with respect to both adhesion and resistance to cracking. The higher resistance to cracks and spalling shown by the harder coating indicates a higher coating cohesion compared to for the softer coating. The results from the microabrasion experiment using 6 μm diamonds are in disagreement with the results from the scratch testing. This can be explained by considering the following points:

- There was no significant difference in friction coefficient between the indenter and the coatings.

- The harder coating had a greater load-bearing characteristic, which prevented the indenter to penetrate into the coating.
- The harder coating had a much higher degree of orientation than the softer coating as described in section 4.3.2. As mentioned in section 4.3.5 this could possibly allow for dislocations moving across the grain boundaries, thus preventing cracking.
- The softer coating underwent a change of orientation during the growth, from $\langle 111 \rangle$ to $\langle 211 \rangle$ and $\langle 311 \rangle$, possibly creating weak spots providing onsets for cracking/spalling.

The difference in surface roughness between the coatings is not believed to influence the scratch testing as the indenter was orders of magnitude larger than the coating roughness. This is confirmed by the negligible difference in friction seen during the scratch testing. The higher degree of orientation implies that there was a smaller misorientation between the grains in the harder coating compared to the softer coating. Therefore, the deformation over two grains was less likely to induce cracks. This was shown in the deformation study, where the $\langle 111 \rangle$ oriented coating exhibited a much lower density of cracks compared to the $\langle 211 \rangle$ oriented coating. Lastly, the orientation interface in the softer coating could act as a mechanically weak area, thus lowering the force required for coating cracking and spalling.

In conclusion, the harder coating shows a rather rare combination of both high hardness and high toughness.

4.5. Corrosion resistance of Ti(C,N)

Chemical inertness is an important property for coatings in cutting applications, since in most cases chemical interactions between the coating and the work material are undesirable. In addition to be used in metal cutting, Ti(C,N) coatings show promise both in biomechanical applications and in corrosion protection. Electrochemical measurements are good tools to investigate both the corrosion resistance and the chemical inertness. The corrosion properties and chemical inertness were investigated for the Ti(C,N) coating, deposited using a high N_2 partial pressure (sample 4, **Table 2**). This was investigated by potentiodynamic polarization in an artificial sea water environment (i.e. 3.5 %wt. NaCl).

The polarization curve is shown in **Figure 35**. It is seen that from -0.3 V, the current increased until reaching a local maxima at 0.32 V. A further increase of the potential caused the current to decrease up to a potential of roughly 0.68 V after which the current increased. A second maximum was observed at 1.05 V, after which a plateau was reached. Upon further poten-

tial increase the current increased steadily. The presence of two local maxima indicates a dual passivation behavior.

Two TiC and a TiN coatings were further analyzed to investigate the origin of the passivations, see **Figure 35**. For the deposition details on the TiC and TiN coatings, see paper VI Appendix 1. The polarization of TiC shows similarities to that of Ti(C,N) except at the position of the first peak (i.e. at 0.51 V for TiC). Furthermore, the polarization of the TiC coating resulted in a higher current in the region 0.5 to 0.9 V compared to Ti(C,N). Polarization of TiN resulted in a steady current increase until 1.10 V after which the current remained constant.

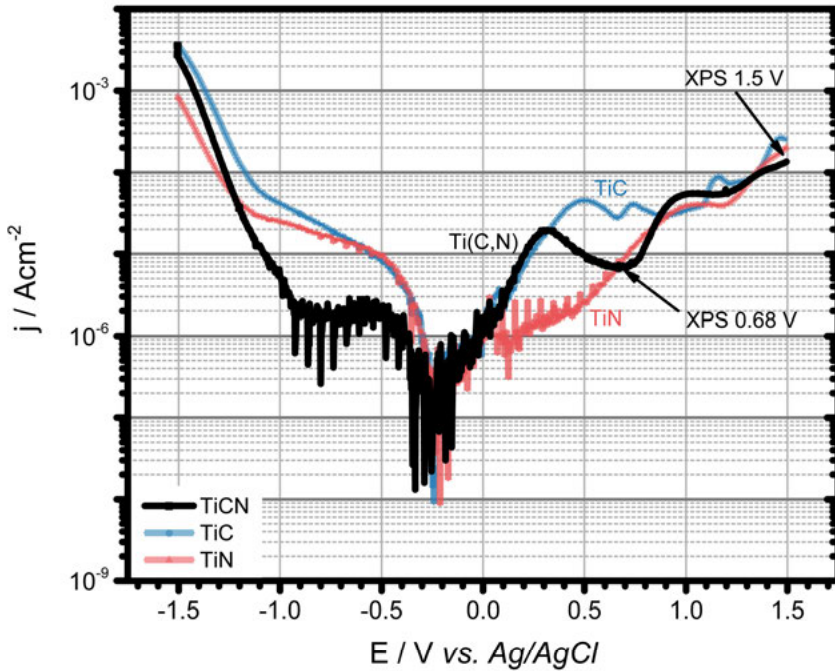
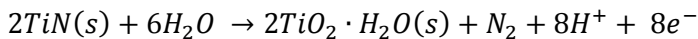
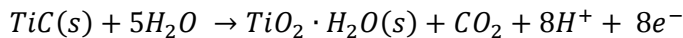


Figure 35. Potentiodynamic polarization curves for Ti(C,N), TiC and TiN coatings in 3.5 wt % NaCl electrolyte. The points where the samples were stopped for XPS analyses are marked.

Based on the polarization curves of TiC and TiN it is most likely that the Ti(C,N) polarization curve is a result of both TiC and TiN oxidation and passivation. Ti(C,N) is oxidized to TiO_2 according to the following reactions for the TiC and TiN oxidation [65,66]:



As the Ti(C,N) coating was shown to be on the carbon-rich side, $\text{Ti}(\text{C}_{0.6},\text{N}_{0.4})_{0.8}$, it was expected that the polarization behavior would be more similar to that of TiC. The first oxidation peak in the polarization curve, both for TiC and Ti(C,N), is associated with the oxidation of TiC to TiO_2 and oxidized carbon species. It has also been speculated in previous investigations that the oxidation of TiC would generate carbonate species on the electrode surface [65]. The multiple passivation peaks observed in the TiC polarization curve indicates several oxidation steps, possibly including carbonate species.

TiN has been shown to oxidize to form TiO_2 and elemental nitrogen[66]. To overcome the passivation and further oxidize the underlying TiN layer an applied potential exceeding 1.05 V seems to be required.

To investigate the passivating layers formed in the polarization of Ti(C,N) XPS was used. Two different stages of polarization were analyzed, as indicated in Figure 35. The XPS analysis of the polarized as well as a reference sample is presented in **Figure 36**. In the Ti 2p spectra, **Figure 36a**, it can be seen that the intensity of the peaks associated with Ti(C,N) at 455.1 and 461.0 eV decrease upon increasing polarization. Two peaks appear at higher binding energies 459.3 and 465.2 eV, which indicates an oxide environment on the surface. This oxide environment most probably corresponds to a thin passivating layer of TiO_2 [92]. Presence of Ti with oxidation state lower than 4+ was also detected for the fully polarized sample.

In the C 1s spectra, **Figure 36c**, peaks corresponding to a carbide environment were found. Upon polarization these peaks decreased in intensity and peaks at higher binding energies, corresponding to oxidized carbon environment, appeared [55,93]. The peak at 289.9 eV most likely corresponds to carbonate species, in agreement the previous hypothesis [55].

The N 1s spectra, see **Figure 36d**, show a reduced intensity of peaks associated with nitride environment upon polarization and a broad feature most likely associated with oxidized nitrogen species at about 400 eV upon polarization at 1.5 V [94]. In accordance with the Ti 2p spectra the O 1s spectra, **Figure 36b**, the peak associated with Ti – O increase in intensity upon polarization, confirming a layer of TiO_2 .

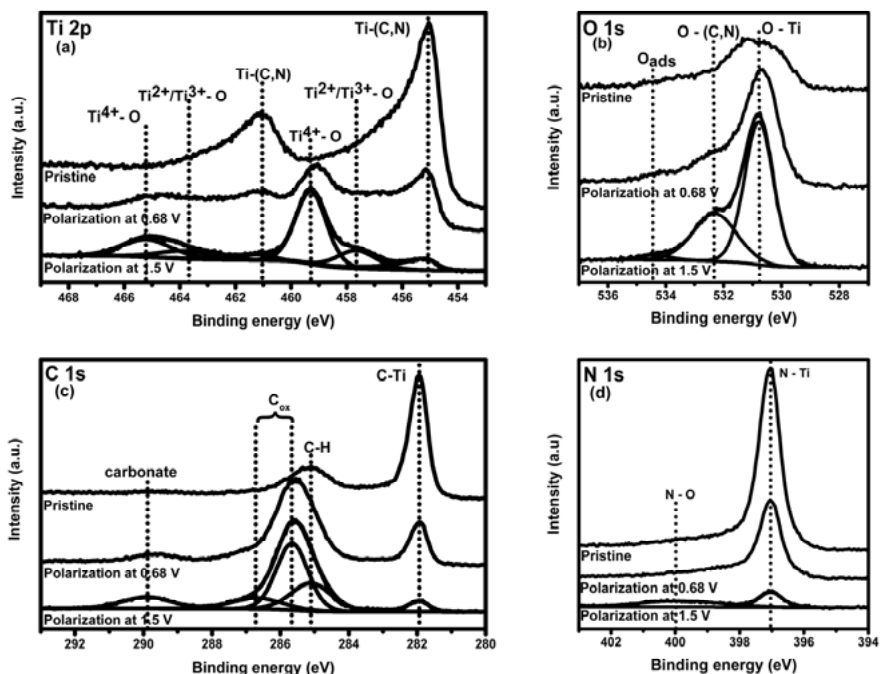


Figure 36. XPS spectra of the core levels of: a) Ti 2p, b) O 1s, c) C 1s and d) N 1s for the Ti(C,N) samples that during the polarization have been stopped at 0.68 and 1.5 V respectively and for a pristine Ti(C,N) reference sample.

The XPS analysis confirms the oxidation of Ti(C,N) into TiO₂. However, since no gas evolution could be observed during the experiments and the individual TiC and TiN corrosion reactions suggested above could not be confirmed. Furthermore, the XPS analysis confirms the hypothesis of carbonates species forming on the electrode surface. Corrosion products such as CO₂ and N₂ are most likely desorbing as gas and therefore not detectable in the XPS analysis.

Additional surface analysis was conducted by AFM and SEM in order to investigate any corrosion effects on the surface. It was found that the effective surface area was unaffected by the corrosion and that the morphology remained intact, see **Figure 37**.

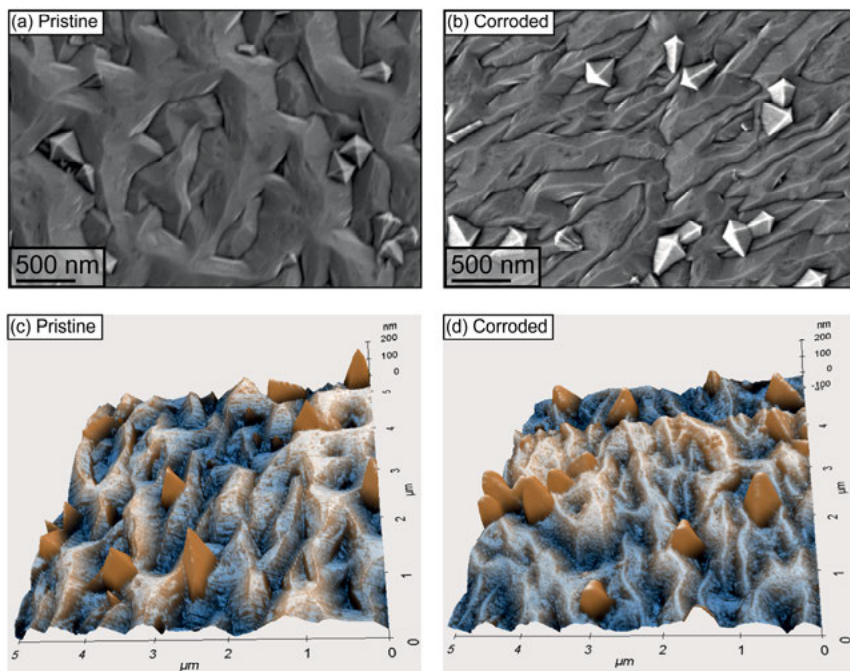


Figure 37. Surface morphology (a and c) before and (b and d) after corrosion, imaged by (a-b) SEM and (c-d) AFM.

In conclusion, the corrosion resistance and chemical inertness of Ti(C,N) coatings is high in artificial sea water. Ti(C,N) undergoes passivation of by formation of a thin passivating TiO_2 film. The formed TiO_2 was stable and prevented dissolution of the coating.

5. Concluding remarks

The work in this thesis has been focused on the deposition and characterization of Ti-based hard coatings for metal cutting applications. Two different coatings were investigated: TiN and Ti(C,N). All coatings were deposited by CVD using industrial-scale reactors. The coatings were characterized using a variety of techniques, e.g. SEM, TEM, XRD, and XPS.

TiN is normally the first layer to be deposited in a multilayer system on a cutting tool and it serves as a nucleation layer for the following layers. As such, it is important to control the microstructure and morphology of this layer to enable controlled growth of the following layers. The composition of the substrate was found to be of great importance for the properties of the deposited TiN layer. Layers deposited on Co substrates attained a dense and homogeneous microstructure and morphology, while layers grown on Fe and Ni substrates behaved differently.

The Fe substrates were corroded by the process gases and gave a porous substrate-coating interface. Such coatings are not desirable in metal cutting applications as porous substrates typically results in poor mechanical properties. To prevent corrosion of Fe based substrates the suggestion is to keep the deposition temperature as low as possible in order to reduce the corrosion rate.

TiN deposition on Ni based substrates proved to be even more complicated than on Fe substrates. It was shown that a majority of the deposited coating contained an intermetallic phase of Ni and Ti (Ni_3Ti) and only small amounts of the desired TiN. The intermetallic phase is unwanted in metal cutting applications as the mechanical properties are poor compared to TiN. The formation of an intermetallic phase could be significantly reduced by adjusting the deposition process. This shows that CVD of TiN on cutting tools containing Fe and Ni needs to be optimized towards the used metal(s) to obtain coatings suitable for metal cutting.

Ti(C,N) is normally the layer deposited on TiN and is most likely affected by the properties (microstructure, morphology and orientation) of the preceding layer. Therefore, it was of interest to study how substrate and process modifications affected the material and mechanical properties of the Ti(C,N) layer.

It was found that Ti(C,N) deposited using CH_3CN as a precursor for both C and N had a strong driving force for formation of fine-grained $\langle 211 \rangle$ oriented coating. The mechanism behind the orientation formation was investi-

gated and it was speculated to be caused by a high $\text{TiCl}_4/\text{CH}_3\text{CN}$ ratio in combination with the strong C-N bonding in the cyanide group of CH_3CN .

Deposition of $\text{Ti}(\text{C},\text{N})$ on single crystal (001) $\alpha\text{-Al}_2\text{O}_3$ substrates enabled deposition of $\langle 111 \rangle$ oriented $\text{Ti}(\text{C},\text{N})$. However, the coatings changed orientation to $\langle 211 \rangle$ despite the epitaxial relation with the substrate. It was found that the $\langle 111 \rangle$ orientation of the $\text{Ti}(\text{C},\text{N})$ coating could be maintained by modifying the $\text{TiCl}_4/\text{CH}_3\text{CN}$ ratio or by replacing H_2 with N_2 . The change in orientation also caused a change in microstructure and morphology to a larger grain size than that of the $\langle 211 \rangle$ oriented coating. In addition, it was found that the hardness of the $\langle 111 \rangle$ oriented coating was significantly higher. The increased hardness of the $\langle 111 \rangle$ oriented coating compared to the $\langle 211 \rangle$ oriented coating was found to be caused by a higher degree of orientation, a more beneficial arrangement of crystallographic slip planes, defect induced surface hardening, and compressive stresses.

The tribological properties and corrosion resistance of $\text{Ti}(\text{C},\text{N})$ coatings was also investigated. It was found that $\langle 111 \rangle$ oriented $\text{Ti}(\text{C},\text{N})$ had a higher resistance to abrasion by small diamond particles and a better adhesion than a $\langle 211 \rangle$ oriented $\text{Ti}(\text{C},\text{N})$. Furthermore, as expected, $\text{Ti}(\text{C},\text{N})$ had a corrosion behavior that was a mixture of those for TiC and TiN oxidation. The surface was passivated by TiO_2 formation, giving $\text{Ti}(\text{C},\text{N})$ a high resistance to corrosion in an artificial sea water environment. This makes $\text{Ti}(\text{C},\text{N})$ an excellent candidate for corrosion protection in mechanically demanding applications.

6. Sammanfattning på svenska

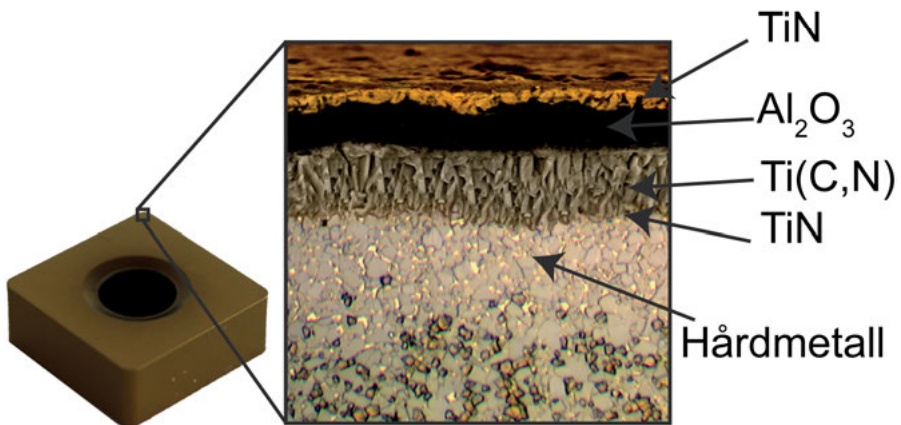
Att förändra egenskaperna hos ett material genom att applicera en tunn ytbeläggning är ett mycket välkänt koncept som har använts i hundratals år. Lacken på en bil är ett typiskt exempel på en ytbeläggning, där lacken bidrar till att skydda mot korrosion utöver att ge en trevlig färg. Typiskt är tjockleken på lacken ca 100 μm (en tiotusendels meter), vilket ungefär motsvarar tjockleken på ett hårstrå.

Skikten som har undersökts i denna doktorsavhandling används till att förbättra egenskaperna hos verktyg som används för att bearbeta metall till exempel genom borrar, svarvning och fräsning. Vid bearbetning av metall uppstår mycket besvärliga förhållanden, så som höga temperaturer, höga tryck och hög friktion. Detta kan leda till mycket snabb förslitning om inte verktygen har rätt egenskaper. Hög hårdhet och hög smältpunkt har visat sig vara mycket viktiga egenskaper för ett skärverktyg. Verktygen som används består oftast av en förening av volfram och kol i en bindefas av kobolt. Volfram och kol (volframkarbid) bidrar till att verktyget får en hög smältpunkt och blir mycket hårt medan kobolt agerar som ett lim och ger seghet, vilket förhindrar att verktyget spricker. Den här typen av verktyg tillverkades i början av 1900 talet och har sedan dess använts flitigt då de håller betydligt längre än vad verktyg av stål gör. På 1960-talet upptäcktes att man kunde förbättra livslängden på verktygen mer än 10 gånger genom att applicera ett tunt skikt bestående av en förening av titan och kol (titankarbid).

Ytbeläggningen tillverkades genom så kallad kemisk gasdeponering (chemical vapor deposition (CVD)), en teknik som låter ämnen i gasfas reagera på en yta och på så vis bilda ett fast material på ytan. Man reducerar alltså en metalljon istället för att smälta metallen. Fördelen är då att man använda sig av en betydligt lägre temperatur. Titankarbid har en smältpunkt på över 3000 °C, vilket gör det besvärligt att tillverka ett skikt från en smälta, då substratet (verktyget) skulle ta skada. Vid CVD av titankarbid möjliggörs deponering vid temperaturer omkring 1000 °C. Vid så pass "låga" temperaturer är verktygsmaterialet stabilt och på så vis kan man tillverka ett skikt utan att skada verktyget.

Kraftigt reaktiva gaser möjliggör ytbeläggning vid temperaturer mycket lägre än materialets smältpunkt. På grund av att gaserna i regel är väldigt reaktiva använder man oftast en vakuumkammare för att undvika oönskade reaktioner med den omgivande luften. På så vis kan man ha en kontrollerad atmosfär i sin reaktor och styra de reaktioner som bidrar till att bilda ytbe-

läggningen. De flesta skärverktyg som säljs har en kombination (multilager) av flera olika beläggningsmaterial. På så vis kan man kombinera de positiva egenskaperna hos flera olika material. Vanligtvis består ett multilager av minst tre olika skiktmaterial, det skikt som läggs först och sist är en kombination av titan och kväve, titannitrid (TiN). Titannitrid bidrar till att efterkommande skikt har en god vidhäftning till verktyget och ger även en vacker guldlikande färg. Nästa skikt som läggs ovanpå titannitriden är en kombination av titannitrid och titankarbid, titankarbonitrid (Ti(C,N)). Titankarbonitriden är mycket hård och bidrar till att öka verktygets slitstyrka. Ovanpå titankarbonitriden läggs oftast ett skikt av aluminiumoxid, vilket är en förening mellan syre och aluminium (Al_2O_3). Aluminiumoxiden är kemiskt väldigt stabil och bidrar till att skärverktyget inte reagerar kemiskt med materialet som bearbetas. Den totala tjockleken på hela multilaget är vanligtvis mellan 10 och 15 μm . Det är alltså ungefär en tiondel av ett hårstrå tjockt och bidrar till att öka verktygets livslängd med 20-30 gånger. Ett exempel på hur tvärsnittet på ett svarvskär kan se ut visas i **Figur 38**.



Figur 38. Exempel på hur beläggningen på ett svarvskär kan vara uppbyggd.

En nackdel med att ha väldigt reaktiva gaser är att de kan interagera med materialet i verktyget och orsaka korrosion och på så vis försämra egenskaperna hos ytbeläggningen. Dagens CVD processer är anpassade för att ha kobolt som bindefas i verktyget. Men koboltpulver som används i tillverkningen av verktygen har negativa hälsoeffekter och misstänks orsaka cancer. Därför vill man gärna byta till en annan metall som inte är lika giftig. Järn och nickel har undersökts som kandidater då de inte uppvisar lika negativa hälsoeffekter som kobolt. En del av undersökningarna som har gjorts i den här avhandlingen behandlar hur ytbeläggningen med titannitrid påverkas när man byter metall i bindefasen.

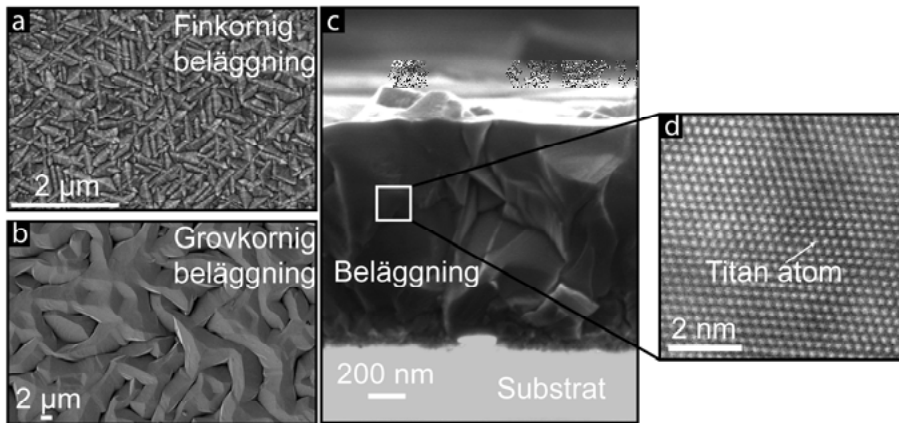
Det visade sig att när man har järn i bindefasen finns det risk för att korrosion uppstår. De beläggningar som gjorts på järnbaserade substrat var porösa och uppvisade tydliga spår av korrosion. Det visar på att järn är mer känsligt än vad kobolt är och att man behöver anpassa sin beläggningsprocess när man har järn i verktyget. När nickel användes som substrat blev effekten en annan: substratet korroderade inte men det bildades en legering mellan nickel och titan (Ni_3Ti). Den legeringen har sämre mekaniska egenskaper än TiN och är därför oönskad. Försök har visat att det gick att minska bildningen av Ni_3Ti drastiskt genom att justera gasfasens sammansättning.

Resultaten från undersökningen med TiN på nickel och järn visar att samma beläggningsprocess inte fungerar för alla bindefas-metaller. Man måste alltså modifiera befintliga processer för att fungera på verktyg med ny bindefas.

Det har visat sig att man kan förbättra ytskiktets egenskaper kraftigt genom att förändra hur yteläggningen växer, d v s hur atomerna staplas. Genom att kontrollera hur atomerna staplas, kan man styra vilken yta som bildas och på så vis få den yta som har de bästa mekaniska egenskaperna. Detta kan åstadkommas på flera sätt, t ex genom att ändra trycket eller temperaturen i reaktorn eller genom att justera gasfasens sammansättning.

Studierna i den här avhandlingen av nästkommande skikt, titankarbonitrid, har visat att beläggningens egenskaper styrs till stor del av två saker: hur stora de bildade kristallerna blir (kornstorlek) och hur atomerna staplar sig (vilken riktning beläggningen växer i). Beläggningar med stora korn och med det tätast packade atomplanet linjerat parallellt med beläggningens yta visade sig ha överlägsna mekaniska egenskaper jämfört med en finkornig beläggning som har samma atomplan i en 90° vinkel mot ytan. Exempel på finkorniga och grovkorniga beläggningar visas i **Figur 39a-c**. En förutsättning för att skiktmaterialen skall ge en förbättring av verktygets prestanda är att de sitter fast, d.v.s. de har god vidhäftning. Den grovkorniga beläggningen visade, förutom förbättrade mekaniska egenskaper, även en bättre vidhäftning till substratet än den finkorniga. De mekaniska förbättringarna kunde förklaras med att rätt atomplan var parallellt med ytan och att det på så vis blir svårare att deformera materialet. Samtidigt leder detta också till att sprickor inte fortplantas lika lätt. Exempel på hur atomplanen staplar sig visas i **Figur 39d**. Den förändrade kornstorleken och riktningen kunde åstadkommas genom att justera flödet på de gaser som används i deponeringen och på så vis förändra gasfasens sammansättning.

Sammantaget visar resultaten i den här avhandlingen att man genom förändringar i kornstorlek och tillväxtriktning hos Ti(C,N)-beläggningar kan få kraftigt förbättrade mekaniska egenskaper.



Figur 39. a och b är exempel på två olika kornstorlekar avbildat med svepelektronmikroskop. Notera den högre förstoringen i a. a) visar en finkornig beläggning, b) visar en grovkornig beläggning, c) tvärsnittet i en grovkornig beläggning avbildat med svepelektronmikroskop, d) visar hur atomerna är linjerade i det inringade området i c, avbildat med transmissionselektronmikroskop.

En mängd olika analystekniker har använts för att undersöka de deponerade materialen. Huvudsakligen har två olika tekniker använts: elektronmikroskopi och röntgendiffraktion. Synonymt för båda teknikerna är att de använder någon typ av strålning som interagerar med provet och genererar en respons som man kan mäta. Elektronmikroskopi använder sig av elektroner som ljuskälla och tack vare elektronens korta våglängd (jämfört med synligt ljus) möjliggörs så höga förstoringar att man kan se enskilda atomer. Alla kornstorlekar och tvärsnitt på beläggningar i den här avhandlingen har undersökts med hjälp av elektronmikroskopi, exempel visas i **Figur 39**.

För att undersöka hur atomplanen staplas använder man sig av röntgendiffraktion där röntgenstrålar används som ljuskälla. Beroende på hur atomplanen staplas genereras olika mönster och man kan på så vis avgöra vilket eller vilka atomplan som växer.

7. Acknowledgements

Till att börja med vill jag rikta ett stort tack till min huvudhandledare Mats Boman, för en mycket inspirerande och uppmuntrande handledning samt kullinariska upplevelser utöver det vanliga. Jag hoppas på fler GT-provningar i Bisen framöver. Jag vill även rikta ett tack till min biträdande handledare Ulf Jansson för allt stöd och all hjälp under åren. Jag vill även passa på att tacka mina biträdande handledare från industrin, Erik Lindahl och Jeanette Persson från Sandvik och Tommy Larsson från Seco. Ni har betytt oerhört mycket för mig och er hjälp och stöttning har varit helt ovärderlig.

Jag vill också passa på att tacka Oscar och Jonas för all hjälp och bra diskussioner. Jag vill också tacka: Janne E, Olof B, Mikael F, Gunnar, Lars-Anders B och Fredrik W för all hjälp. Därtill vill jag tacka AB Sandvik Coromant som möjliggjort dessa studier genom finansiering och nyttjande av processutrustning.

Timmy och Johan (Tård), ni fanns där när det var som tyngst, ni anar inte hur tacksam jag är för allt ni gjort för mig, jag hade inte klarat det är utan er! David, vi har suttit ihop sedan dag 1 (HT06) vi har gjort det mesta tillsammans under alla dessa år, allt ifrån omentor till kemishower, it has been a blast ☺. I would also like to thank the rest of "Kaffe gruppen": Sarmad, Kristina, Gerd, Ernesto and Stefan, you guys are the best!

There are many other co-workers at Chemistry Ångström I would like to thank for creating a nice work environment and nice coffee breaks, thanks to all of you.

I would also like to send a special thanks to my brother from another mother, Fabian. One cannot hope for a better office buddy and roommate. Unfortunately Das Kontor will close for good now, but it was the most awesome after works ever and the legend will live on for generations ☺

My sincerest and greatest thanks to Will Brant for proofreading my manuscripts!

Jag vill rikta ett stort tack till hela min familj, för allt stöd och all uppmuntran. Frans, du är inte bara min bror, du är även min bästa vän, det går inte att förklara hur mycket du har betytt för mig under hela mitt liv. Tack för att du alltid finns där!

Kristina, jag hade inte klarat detta utan dig, du har hjälpt mig så otroligt mycket med allt och finns alltid där när det är som tyngst, du är helt enkelt bäst!

8. References

- [1] Early Stone Age Tools The Smithsonian Institution's Human Origins Program, (n.d.). <http://humanorigins.si.edu/evidence/behavior/stone-tools/early-stone-age-tools>.
- [2] S. Norgren, J. García, A. Blomqvist, L. Yin, Trends in the P/M hard metal industry, *Int. J. Refract. Met. Hard Mater.* 48 (2015) 31–45. doi:10.1016/j.ijrmhm.2014.07.007.
- [3] M. Ibrahim Sadik, *An introduction to cutting tools materials and applications*, 1st ed., Elanders, Sweden, 2013.
- [4] K. Schröter, Patent Hard-metal alloy and the process of making same, 1,549,615, 1923.
- [5] W. Schintlmeister, W. Wallgram, J. Kanz, S. Diego, Properties, applications and manufacture of wear-resistant hard material coatings for tools*, *Thin Solid Films.* 107 (1983) 117–127.
- [6] L.F. Pochet, P. Howarda, S. Safaieb, CVD coatings : from cutting tools to aerospace applications and its future potential, *Surf. Coat. Technol.* 95 (1997) 70–75.
- [7] H.E. Rebenne, D.G. Bhat, Review of CVD TiN coatings for wear-resistant applications: deposition processes, properties and performance, *Surf. Coatings Technol.* 63 (1994) 1–13. doi:10.1016/S0257-8972(05)80002-7.
- [8] R. M'Saoubi, O. Alm, J.M. Andersson, H. Engström, T. Larsson, M.P. Johansson-Jöesaar, M. Schwind, Microstructure and wear mechanisms of texture-controlled CVD α -Al₂O₃ coatings, *Wear.* 376–377 (2017) 1766–1778. doi:10.1016/j.wear.2017.01.071.
- [9] M. Fallqvist, M. Olsson, S. Rупpi, Abrasive wear of texture-controlled CVD α -Al₂O₃ coatings, 202 (2007) 837–843. doi:10.1016/j.surfcoat.2007.06.063.
- [10] J. Todt, J. Zalesak, R. Daniel, R. Pitonak, A. Köpf, R. Weißenbacher, B. Sartory, C. Mitterer, J. Keckes, Al-rich cubic Al_{0.8}Ti_{0.2}N coating with self-organized nano-lamellar microstructure: Thermal and mechanical properties, *Surf. Coatings Technol.* 291 (2016) 89–93. doi:10.1016/j.surfcoat.2016.02.027.
- [11] I. Endler, M. Höhn, M. Herrmann, R. Pitonak, S. Rупpi, M. Schneider, H. Van Den Berg, H. Westphal, Surface & Coatings Technology Novel aluminum-rich Ti_{1-x}Al_xN coatings by LPCVD, *Surf. Coat. Technol.* 203 (2008) 530–533. doi:10.1016/j.surfcoat.2008.04.098.
- [12] R. Bonetti, H. Wiprächtiger, E. Mohn, CVD of titanium carbonitride at moderate temperature: Properties and applications, *Met. Powder Rep.* (1990) 837–840.
- [13] J.E. Sundgren, Structure and properties of TiN coatings, *Thin Solid Films.* 128 (1985) 21–44. doi:0040-6090.
- [14] J. Garcia, R. Pitonak, L. Agudo, A. Kostka, Synthesis of titanium carbonitride coating layers with star-shaped crystallite morphology, *Mater. Lett.* 68 (2012) 71–74. doi:10.1016/j.matlet.2011.10.008.

- [15] J. Garcia, R. Pitonak, R. Weissenbacher, A. Köpf, Production and characterization of wear resistant Ti(C,N) coatings manufactured by modified chemical vapor deposition process, *Surf. Coatings Technol.* 205 (2010) 2322–2327. doi:10.1016/j.surfcoat.2010.09.013.
- [16] A. Paseuth, H. Fukui, K. Yamagata, Surface & Coatings Technology Improvement of mechanical properties and cutting performance of modified MT-TiC_xN_{1-x} coating by moderate temperature chemical vapor deposition, *Surf. Coat. Technol.* 291 (2016) 54–61. doi:10.1016/j.surfcoat.2016.02.023.
- [17] A. Paseuth, H. Fukui, S. Okuno, H. Kanaoka, Y. Okada, Microstructure, mechanical properties, and cutting performance of TiC_xN_{1-x} coatings with various x values fabricated by moderate temperature chemical vapor deposition, *Surf. Coatings Technol.* 260 (2014) 139–147. doi:10.1016/j.surfcoat.2014.09.068.
- [18] W. Schintlmeister, Patent Coated cemented carbide elements, 4,101,703, 1975.
- [19] E.N. Smith, L.F. Pochet, Patent Sintered cemented carbide body coated with three layers, 4,035,541, 1977.
- [20] L. Wang, W. Jiang, L. Chen, M. Yang, H. Zhu, Consolidation of Nano-Sized TiN Powders by Spark Plasma Sintering, *J. Am. Ceram. Soc.* 89 (2006) 2364–2366. doi:10.1111/j.1551-2916.2006.01066.x.
- [21] S. Urbonaite, M. Johnsson, G. Svensson, Synthesis of TiC_{1-x}N_x and TaC_{1-x}N_x by spark plasma sintering, *J. Mater. Sci.* 39 (2004) 1907–1911.
- [22] S. Jin, P. Shen, Q. Lin, L. Zhan, Q. Jiang, Growth Mechanism of TiC_x during Self-Propagating High-Temperature Synthesis in an Al–Ti–C System, *Cryst. Growth Des.* 10 (2010) 1590–1597. doi:10.1021/cg9010983.
- [23] Y. Xu, X.-T. Yan, *Chemical Vapour Deposition*, Springer London, London, 2010. doi:10.1007/978-1-84882-894-0.
- [24] A. Kafizas, C.J. Carmalt, I.P. Parkin, CVD and precursor chemistry of transition metal nitrides, *Coord. Chem. Rev.* 257 (2013) 2073–2119. doi:10.1016/j.ccr.2012.12.004.
- [25] K. Choy, Chemical vapour deposition of coatings, *Prog. Mater. Sci.* 48 (2003) 57–170. doi:10.1016/S0079-6425(01)00009-3.
- [26] J. Carlsson, *Chemical Vapor Deposition, Handb. Depos. Technol. Film. Coatings.* (2010) 400–459. doi:10.1016/B978-0-8155-2031-3.00007-7.
- [27] M.H. Staia, Microstructural characterization of chemically vapor deposited TiN coating, *Surf. Coatings Technol.* 86–87 (1996) 432–437.
- [28] A. Sherman, Growth and properties of LPCVD titanium nitride as a diffusion barrier for silicon device technology, *J. Electrochem. Soc.* 137 (1990) 1892–1897. doi:10.1149/1.2086826.
- [29] H. Holleck, Material selection for hard coatings Material selection for hard coatings, *J. Vac. Sci. Technol. A Vacuum, Surfaces, Film.* 4 (1986) 2661–2669. doi:10.1116/1.573700.
- [30] K. Akiyama, E. Nakamura, I. Suzuki, T. Oshika, A. Nishiyama, Y. Sawada, A study of the adhesion between CVD layers and a cemented carbide substrate by AEM analysis, *Surf. Coatings Technol.* 94–95 (1997) 328–332. doi:10.1016/S0257-8972(97)00441-6.
- [31] S.J. Bull, D.G. Bhat, M.H. Staia, Properties and performance of commercial TiCN coatings. Part 2: Tribological performance, *Surf. Coatings Technol.* 163–164 (2003) 507–514. doi:10.1016/S0257-8972(02)00651-5.

- [32] S. Bastian, W. Busch, D. Kühnel, A. Springer, T. Meißner, R. Holke, S. Scholz, M. Iwe, W. Pompe, M. Gelinsky, A. Potthoff, V. Richter, C. Ikonomidou, K. Schirmer, Toxicity of tungsten carbide and cobalt-doped tungsten carbide nanoparticles in mammalian cells in vitro, *Environ. Health Perspect.* 117 (2009) 530–535. doi:10.1289/ehp.0800121.
- [33] V. Richter, A. Potthoff, W. Pompe, M. Gelinsky, H. Ikonomidou, S. Bastian, K. Schirmer, S. Scholz, J. Hofinger, Evaluation of health risks of nano- and microparticles, *Powder Metall.* 51 (2008) 8–9. doi:10.1179/174329008X286640.
- [34] L. Toller, C. Liu, E. Holmström, T. Larsson, S. Norgren, Investigation of cemented carbides with alternative binders after CVD coating, *Int. J. Refract. Met. Hard Mater.* 62 (2017) 225–229. doi:10.1016/j.ijrmhm.2016.07.005.
- [35] L. Toller, S. Jacobson, S. Norgren, Life time of cemented carbide inserts with Ni-Fe binder in steel turning, *Wear.* 376–377 (2017) 1822–1829. doi:10.1016/j.wear.2017.02.018.
- [36] M.H. Staia, B. Lewis, J. Cawley, T. Hudson, Chemical vapour deposition of TiN on stainless steel, *Surf. Coatings Technol.* 76–77 (1995) 231–236. doi:10.1016/0257-8972(95)02527-8.
- [37] W. Schintlmeister, Structure and Strength Effects in CVD Titanium Carbide and Titanium Nitride Coatings, *J. Electrochem. Soc.* 123 (1976) 924. doi:10.1149/1.2132969.
- [38] J.C. Nable, S. Nosheen, S.L. Suib, F.S. Galasso, Atmospheric pressure chemical vapor deposition of titanium nitride on metals, *Surf. Coatings Technol.* 200 (2006) 2821–2826. doi:10.1016/j.surfcoat.2005.02.171.
- [39] I.Y. Konyashin, Wear-resistant coatings for cermet cutting tools, *Surf. Coatings Technol.* 71 (1995) 284–291. doi:10.1016/0257-8972(94)02326-L.
- [40] H.J.L. Van der Valk, J.H.F. Grondel, Chemical vapour deposition of titanium diboride on metallic substrates, *Solid State Ionics.* 16 (1985) 99–104.
- [41] P.C. Jindal, A.T. Santhanam, U. Schleinkofer, A.F. Shuster, Performance of PVD TiN, TiCN, and TiAlN coated cemented carbide tools in turning, *Int. J. Refract. Met. Hard Mater.* 17 (1999) 163–170. doi:10.1016/S0263-4368(99)00008-6.
- [42] F. Hollstein, P. Louda, Bio-compatible low reflective coatings for surgical tools using reactive d.c.-magnetron sputtering and arc evaporation - a comparison regarding steam sterilization resistance and nickel diffusion, *Surf. Coatings Technol.* 120–121 (1999) 672–681. doi:10.1016/S0257-8972(99)00357-6.
- [43] N. Madaoui, N. Saoula, B. Zaid, D. Saidi, A.S. Ahmed, Structural, mechanical and electrochemical comparison of TiN and TiCN coatings on XC48 steel substrates in NaCl 3.5% water solution, *Appl. Surf. Sci.* 312 (2014) 134–138. doi:10.1016/j.apsusc.2014.04.167.
- [44] F. Odell, Phase Relationships in the Binary Systems of Nitrides and Carbides of Zirconium, Columbium, Titanium, and Vanadium, *J. Electrochem. Soc.* 97 (1950) 299–304.
- [45] E. Kübel, New developments in chemically vapour-deposited coatings from an industrial point of view, *Surf. Coatings Technol.* 49 (1991) 268–274. doi:10.1016/0257-8972(91)90067-7.
- [46] A. Larsson, S. Rupp, Microstructure and properties of Ti(C,N) coatings produced by moderate temperature chemical vapour deposition, *Thin Solid Films.* 402 (2002) 203–210. doi:10.1016/S0040-6090(01)01712-6.
- [47] K. Holmberg, A. Matthews, *Coatings Tribology*, 2nd ed., Elsevier B.V., Amsterdam, 2009.

- [48] B. Noläng, Computer program Ekvivalc 4.6, Öornsätra, S-74386 Bälänge, Sweden, (1982).
- [49] M. Birkholz, Thin Film Analysis by X-Ray Scattering, Wiley-VCH Verlag GmbH & Co. KGaA, Weinheim, 2006.
- [50] R.F. Egerton, Physical Principles of Electron Microscopy, 1st ed., Springer US, Boston, MA, 2005. doi:10.1007/b136495.
- [51] D.B. Williams, C.B. Carter, Transmission Electron Microscopy, Springer, 2009. doi:10.1007/978-0-387-76501-3_1.
- [52] R.M. Langford, C. Clinton, In situ lift-out using a FIB-SEM system., *Micron*. 35 (2004) 607–11. doi:10.1016/j.micron.2004.03.002.
- [53] M. Schaffer, B. Schaffer, Q. Ramasse, Ultramicroscopy Sample preparation for atomic-resolution STEM at low voltages by FIB, *Ultramicroscopy*. 114 (2012) 62–71. doi:10.1016/j.ultramic.2012.01.005.
- [54] J.;Shau. W. Brundle, C. Richard;Charles A. Evans, *Materials Characterization*, 1992. doi:10.1002/9783527670772.
- [55] J.F. Moulder, W.F. Stickle, P.E. Sobol, K.D. Bomben, *Handbook of X-ray Photoelectron Spectroscopy*, Physical Electronics, Inc., Eden Prairie, Minesota, 1992.
- [56] W.C. Oliver, G.M. Pharr, An improved technique for determining hardness and elastic modulus using load and displacement sensing indentation experiments, *J. Mater. Res.* 7 (1992) 1564–1583. doi:10.1557/JMR.1992.1564.
- [57] H. Çalışkan, Effect of test parameters on the micro-abrasion behavior of PVD CrN coatings, *Measurement*. 55 (2014) 444–451. doi:10.1016/j.measurement.2014.05.036.
- [58] P.J. Burnett, D.S. Rickerby, The relationship between hardness and scratch adhesion*, *Thin Solid Films*. 154 (1987) 403–416.
- [59] P.C. Jindal, D.T. Quinto, G.J. Wolfe, Adhesion Measurement of chemically vapor deposited and physically vapor deposited hard coatings on WC-Co substrates, *Thin Solid Films*. 154 (1987) 361–375.
- [60] A.J. Perry, Scratch adhesion testing of hard coatings, *Thin Solid Films*. 107 (1983) 167–180.
- [61] A.J. Perry, J. Valli, P.A. Steinmann, Adhesion scratch testing: A round-robin experiment, *Surf. Coatings Technol.* 36 (1988) 559–575. doi:10.1016/0257-8972(88)90182-X.
- [62] H.E. Hintermann, Exploitation of wear- and corrosion-resistant cvd-coatings, *Tribol. Int.* 13 (1980) 267–277. doi:10.1016/0301-679X(80)90090-0.
- [63] K.T. Rie, A. Gebauer, J. Wöhle, Plasma assisted CVD for low temperature coatings to improve the wear and corrosion resistance, *Surf. Coatings Technol.* 86–87 (1996) 498–506. doi:10.1016/S0257-8972(96)03177-5.
- [64] T.A. Mantyla, P.J. Helevirta, T.T. Lepisto, P.T. Sitonen, Corrosion behaviour and protective quality of TiN coatings, *Thin Solid Films*. 126 (1985) 275–281.
- [65] B. Beverskog, C.J. O, A. Deblanc Bauer, Corrosion properties of TiC films prepared by activated reactive evaporation, *Surf. Coatings Technol.* 41 (1990) 221–229.
- [66] J. Piippo, B. Elsener, H. Böhni, Electrochemical characterization of TiN coatings, *Surf. Coatings Technol.* 61 (1993) 43–46. doi:10.1016/0257-8972(93)90200-8.
- [67] R. Chatterjee-Fischer, P. Mayr, Investigations on TiCN - layers obtained at moderate temperatures, in: *Proc. Fifth Eur. Conf. Chem. Vap. Depos.*, 1985: pp. 395–405.

- [68] H.-E. Cheng, M.-H. Hon, Texture formation in titanium nitride films prepared by chemical vapor deposition, *J. Appl. Phys.* 79 (1996) 8047. doi:10.1063/1.362358.
- [69] H. Sellers, J. Anderson, Dissociation and recombination rate constants for N₂ on Cu and Ni group transition metal surfaces, *Surf. Sci.* 475 (2001) 11–17. doi:10.1016/S0039-6028(00)00969-9.
- [70] J. Herzler, P. Roth, Shock Tube Study of the Reaction of H Atoms with TiCl₄, *J. Phys. Chem. A.* 101 (1997) 9341–9343. doi:10.1021/jp9718414.
- [71] J. Herzler, P. Roth, High-temperature decomposition of TiCl₄ based on Cl-concentration measurements, *Proc. Combust. Inst.* 29 (2002) 1353–1359. doi:10.1016/S1540-7489(02)80166-3.
- [72] Nakanishi N, S. Mori, E. Kato, Kinetics of Chemical Vapor Deposition of Titanium Nitride, *J. Electrochem. Soc.* 137 (1990) 322–328.
- [73] H.E. Hintermann, L. Suisse, D.R. Horlogkres, S. Francisco, The rate of chemical vapor deposition of TiC, *Thin Solid Films.* 40 (1977) 81–88.
- [74] D.H. Kuo, K.W. Huang, Kinetics and microstructure of TiN coatings by CVD, *Surf. Coatings Technol.* 135 (2001) 150–157. doi:10.1016/S0257-8972(00)00986-5.
- [75] C. Björmander, Coated cutting tool and method of manufacturing the same, EP 2 604 720 A1, 2013.
- [76] G. Ertl, Primary steps in catalytic synthesis of ammonia, *J. Vac. Sci. Technol. A Vacuum, Surfaces, Film.* 1 (1983) 1247–1253. doi:10.1116/1.572299.
- [77] E.A. Hauptfear, L.D. Schmidt, Kinetics and Multiple Steady States in the Chemical Vapor Deposition of Titanium Carbide, *J. Electrochem. Soc.* 140 (1993) 1793–1801.
- [78] J. Emmerlich, H. Högberg, S. Sasvári, P.O.Å. Persson, L. Hultman, J.P. Palmquist, U. Jansson, J.M. Molina-Aldareguia, Z. Czigány, Growth of Ti₃SiC₂ thin films by elemental target magnetron sputtering, *J. Appl. Phys.* 96 (2004) 4817–4826. doi:10.1063/1.1790571.
- [79] T. Törndahl, J. Lu, M. Ottosson, J.-O. Carlsson, Epitaxy of copper on α -Al₂O₃(001) by atomic layer deposition, *J. Cryst. Growth.* 276 (2005) 102–110. doi:10.1016/j.jcrysgro.2004.10.153.
- [80] S. Canovic, B. Ljungberg, M. Halvarsson, CVD TiC/alumina multilayer coatings grown on sapphire single crystals., *Micron.* 42 (2011) 808–18. doi:10.1016/j.micron.2011.05.003.
- [81] S. Canovic, B. Ljungberg, C. Björmander, M. Halvarsson, CVD TiC/alumina and TiN/alumina multilayer coatings grown on sapphire single crystals, *Int. J. Refract. Met. Hard Mater.* 28 (2010) 163–173. doi:10.1016/j.ijrmhm.2009.08.001.
- [82] P.L. Hagans, X. Guo, I. Chorkendorff, A. Winkler, Adsorption and dissociation of HCN on the Pt(111) and Pt(112) surfaces, *Surf. Sci.* 203 (1988) 1–16.
- [83] H. Holzschuh, Chemical-vapor deposition of wear resistant hard coatings in the Ti-B-C-N system: Properties and metal-cutting tests, *Int. J. Refract. Met. Hard Mater.* 20 (2002) 143–149. doi:10.1016/S0263-4368(02)00013-6.
- [84] H. Chien, M.C. Gao, H.M. Miller, G.S. Rohrer, Z. Ban, P. Prichard, Y. Liu, Microtexture and hardness of CVD deposited α -Al₂O₃ and TiC_xN_{1-x} coatings, *Int. J. Refract. Met. Hard Mater.* 27 (2009) 458–464. doi:10.1016/j.ijrmhm.2008.09.010.

- [85] S.J. Bull, D.G. Bhat, M.H. Staia, Properties and performance of commercial TiCN coatings. Part 1: Coating architecture and hardness modelling, *Surf. Coatings Technol.* 163–164 (2003) 499–506. doi:10.1016/S0257-8972(02)00650-3.
- [86] W.D.J. Callister, *Materials Science and Engineering An Introduction*, 7th ed., John Wiley & Sons Inc., 2007.
- [87] L. Karlsson, L. Hultman, M.P. Johansson, J.-E. Sundgren, H. Ljungerantz, Growth, microstructure, and mechanical properties of arc evaporated $\text{TiC}_x\text{N}_{1-x}$ ($0 \leq x \leq 1$) films, *Surf. Coatings Technol.* 126 (2000) 1–14. doi:10.1016/S0257-8972(00)00518-1.
- [88] F.R. Chien, X.J. Ning, A.H. Heuer, Slip systems and dislocation emission from crack tips in single crystal TiC at low temperatures, *Acta Mater.* 44 (1996) 2265–2283. doi:10.1016/1359-6454(95)00360-6.
- [89] N. Li, S.K. Yadav, X.-Y. Liu, J. Wang, R.G. Hoagland, N. Mara, A. Misra, Quantification of dislocation nucleation stress in TiN through high-resolution in situ indentation experiments and first principles calculations, *Sci. Rep.* 5 (2015) 15813. doi:10.1038/srep15813.
- [90] W. Hosford, *Mechanical Behavior of Materials*, 2nd ed., Cambridge University Press, Cambridge, 2009.
- [91] J.C.A. Batista, M.C. Joseph, C. Godoy, A. Matthews, Micro-abrasion wear testing of PVD TiN coatings on untreated and plasma nitrided AISI H13 steel, *Wear.* 249 (2001) 971–979. doi:10.1016/S0043-1648(01)00833-X.
- [92] N.C. Saha, H.G. Tompkins, Titanium nitride oxidation chemistry : An X-ray photoelectron spectroscopy study, *J. Appl. Phys.* 72 (1992) 3072–3079. doi:10.1063/1.351465.
- [93] M.C. Biesinger, L.W.M. Lau, A.R. Gerson, R. St. C. Smart, Applied Surface Science Resolving surface chemical states in XPS analysis of first row transition metals , oxides and hydroxides : Sc , Ti , V , Cu and Zn, *Appl. Surf. Sci.* 257 (2010) 887–898. doi:10.1016/j.apsusc.2010.07.086.
- [94] P.-Y. Jouan, M.-C. Peignon, C. Cardinaud, G. Lempérière, Characterisation of TiN coatings and of the TiN/Si interface by X-ray photoelectron spectroscopy and Auger electron spectroscopy, *Appl. Surf. Sci.* 68 (1993) 595–603.

Acta Universitatis Upsaliensis

*Digital Comprehensive Summaries of Uppsala Dissertations
from the Faculty of Science and Technology 1609*

Editor: The Dean of the Faculty of Science and Technology

A doctoral dissertation from the Faculty of Science and Technology, Uppsala University, is usually a summary of a number of papers. A few copies of the complete dissertation are kept at major Swedish research libraries, while the summary alone is distributed internationally through the series Digital Comprehensive Summaries of Uppsala Dissertations from the Faculty of Science and Technology. (Prior to January, 2005, the series was published under the title “Comprehensive Summaries of Uppsala Dissertations from the Faculty of Science and Technology”.)

Distribution: publications.uu.se
urn:nbn:se:uu:diva-335907



ACTA
UNIVERSITATIS
UPSALIENSIS
UPPSALA
2018